

---

## **CHAPTER 2**

*Measurement of Particle Velocity, Size and Flux by Shadow  
Doppler Velocimetry*

---

## 2.1 Background

Shadow Doppler velocimetry (SDV) is a novel imaging technique for sizing particles of arbitrary shape and arbitrary refractive index and was first proposed by Hardalupas *et al.* (1994). The method is based on the collection of the light diffracted by a particle illuminated by two laser beams<sup>1</sup>, thus the term “shadow”<sup>2</sup>, from which the cross-sectional area of the particle can be directly measured.

In contrast to existing sizing methods based on the collection of diffracted laser light scattered by a particle which were reviewed in Chapter 1, such as that of Orfanoudakis (1994), SDV is not amplitude-based as explained below. The independence of the method from the amplitude of diffractively-scattered light means that no elaborate calibration of an instrument based on the technique is required before measurements, and reliable results can be obtained in *confined* two-phase *reacting* flows, where it is necessary to access the flow through optical windows which are susceptible to particle accretion and random movements due to thermal stresses developed on the surrounding metal parts confining the flow. In addition, particle mass flux measurements of accuracy higher than those obtained, for example, with amplitude-based sizing techniques or phase Doppler anemometry can be made due to the strictly geometrical definition of the area of the sampling space, through which flux is measured, in contrast to the irradiance-dependent estimation of the effective probe volume in phase Doppler systems. More details on the method and the accuracy of the measurement of particle mass flux are presented in §2.6.

## 2.2 Optical Arrangement

The generic optical setup of the SDV instrument used in the present work is presented in figure 2.1. The transmitting optics were those of a conventional laser Doppler velocimeter and consisted of an Ar<sup>+</sup> laser operating at 488 nm and power output of 200-700 mW and a beam-splitter and optical shifter unit which in the present work was a commercial system (Model DISA 55X, DANTEC A/S) with optical frequency shifting provided by a single Bragg cell.<sup>3</sup> The beams were focused by a *f*/600 singlet and formed the LDV probe volume. The collection

---

<sup>1</sup> The method is independent of the number of laser beams by which a particle is illuminated and in its simplest form only one beam can be used (see, for example, figure 10.1 of Hecht 1987). An arrangement where the two beams of a laser Doppler velocimeter are used offers the advantage that two components of particle velocity and the particle mass flux can be simultaneously measured. In addition, particle location in the probe volume relative to the focus of the receiving optics can be measured.

<sup>2</sup> The same way the shadow behind objects is formed when they are illuminated by non-coherent polychromatic light, such as sunlight. In such a case, the total dark shadow behind an object is called “umbra”, whilst the lighter shadow surrounding the “umbra” is called “penumbra”.

<sup>3</sup> Initially a diffraction-grating-based unit was used but the small size of the resulting LDV probe volume and non-uniform irradiance distribution in the probe volume made the measurements difficult and that unit was abandoned.

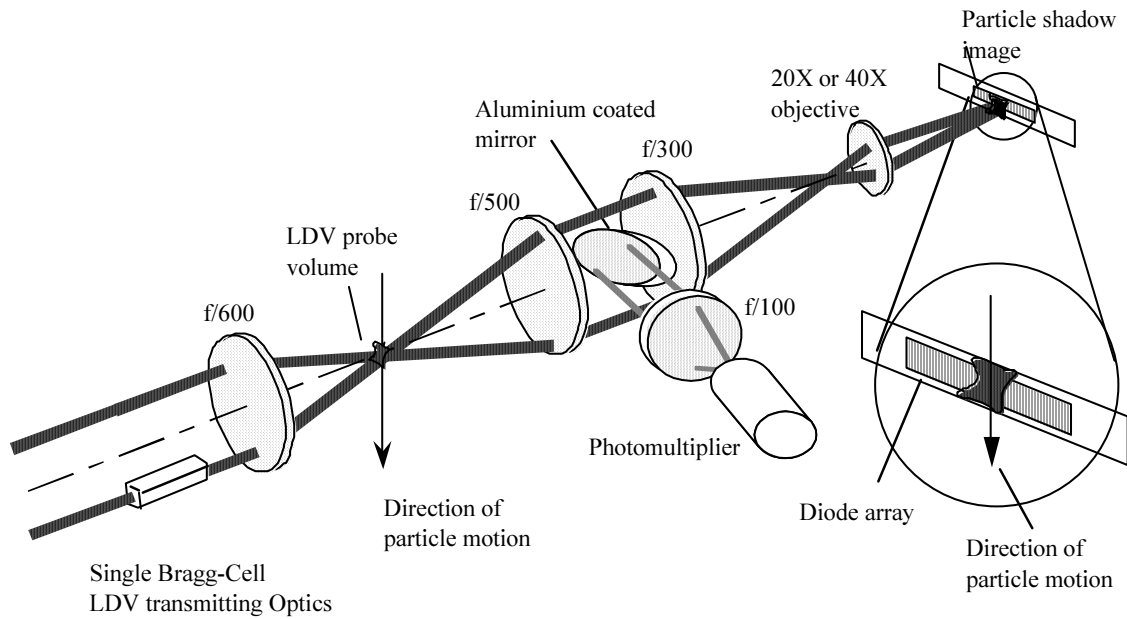


Figure 2.1 Optical setup of the shadow Doppler velocimeter instrument.

optics<sup>4</sup> consisted of an 80 mm-diameter  $f/500$  (Melles Griot Inc., USA) and an 82 mm  $f/300$  (Spindler & Hoyer GmbH & Co., Germany) achromats which collected and focused the laser beams respectively on an 40X microscope objective lens (Edmund Scientific Co., USA), interchangeable with other lenses of smaller magnification ratios. The focal plane of the  $f/500$  lens was on the intersection region of the two laser beams. A 25x35 mm aluminium-coated elliptical mirror was placed behind the  $f/500$  lens and reflected part of the collected light which was subsequently focused on a photomultiplier for the measurement of particle velocity<sup>5</sup>. The purpose of the microscope objective lens was to magnify the image of the LDV probe volume and to project it onto a linear photodiode array (Model S4114-35, Hamamatsu Corp., Japan)<sup>6</sup>. A linear photodiode array was selected as detector in the present implementation of the instrument because it offered the advantage over CCD cameras of high sampling rates, and smaller amount of information for processing, which were required for measurements in the velocity ranges encountered in the flow configurations of this work.

The total optical magnification of the collection optics, which was experimentally determined from measurement of the size of the image of a 100  $\mu\text{m}$  pinhole placed at the centre of the LDV probe volume on the detector plane, was not only a function of the focal lengths of the lenses and the magnification factor of the microscope objective lens, but also an indefinitely

<sup>4</sup>The collection optics for the combined SDV/two-colour pyrometer instrument were a modified version of those presented in this section and will be described later.

<sup>5</sup>In this thesis modifications have been applied to the optical setup for the purpose of simultaneous measurement of particle velocity, size, flux and temperature and these are presented in Chapter 3.

<sup>6</sup>As manufactured, the linear array has 35 diode segments. The current SDV instrument only uses 32 segments and, hence, the array is referred to as a "32-diode array".

increasing function of the distance between the objective lens and the image plane, where the linear photodiode array was placed. The magnification ratio prescribed the dynamic sizing range of the instrument as shown in following section, and upon selection of the collection optics from readily available lenses the magnification ratio could be *increased* by moving the photodiode array along the axis of the optics *away* from the objective lens and vice versa.

### 2.3 Appearance of Particle Images on Detector Plane

Before describing the details of the acquisition and processing procedures it is necessary to explain what could be observed by naked eye on the detector plane when a *stationary* particle was placed in the probe volume. The way shadow images appear is important because it prescribed the design of the data processing hardware and the software validation schemes.

For the purposes of explanation, assume that a spherical particle was mounted on a rotatable optical flat with axis of rotation parallel to the beam bisector, which could be traversed along the axis of the probe volume<sup>7</sup>, *i.e.* parallel to the bisector and was located on the volume's centre and the particle was initially kept stationary in the probe volume. The illuminated particle casts a shadow on the detector plane which is equal to the particle cross-sectional area multiplied by the magnification ratio of the receiving optics (see §2.5.1). Figure 2.2 shows the possible images one could observe on the detector plane as a function of axial position along with the temporal signals if particles were moving due to rotation of the flat. The analysis will be initially confined to stationary particles and thus the temporal signals should be ignored.

Provided that the particle was located in the centre of the probe volume, its shadow would appear on the detector plane as a dark region, figure 2.2(a), surrounded by a bright area and the latter corresponds to the laser light which was not blocked by the particle. Assume now that the particle is displaced *off-centre* along the axis of the optics. This displacement distance away from the centre of the probe volume along the optical axis, is called *defocus* throughout this work. Defocusing results in the appearance of *two* particle shadow images on the image plane, as shown in figure 2.2(b), result of illumination of the particle by *two* laser beams. The two shadow images partly overlap and separate gradually with increasing defocus distance until they disappear when the particle is completely outside the probe volume. On the detector plane, figure 2.2(b), the overlapping region appears darker than the remainder and Hardalupas *et al.* (1994) found that the irradiance level on the detector plane measured over the non-overlapping region is half that over the bright region, *i.e.* the region where no shadow was present.

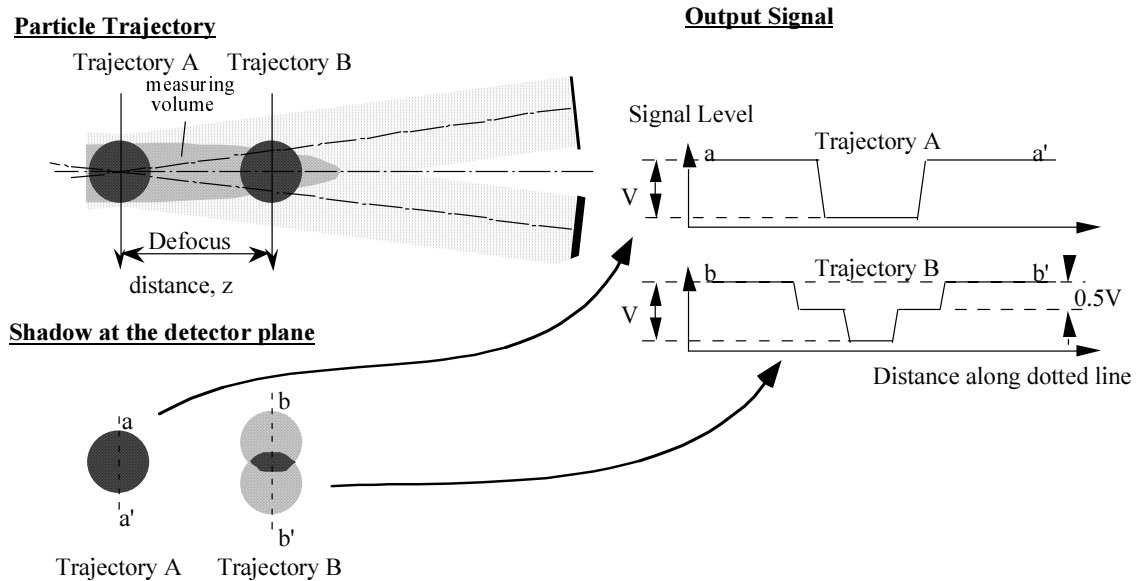


Figure 2.2 Appearance of shadows of spherical particles, moving across the centre of the probe volume, on detector plane as a function of particle trajectory in the LDV probe volume and their respective output signals. The signals are proportional to the irradiance detected from an array diode along the dotted lines ( $aa'$ ) and ( $bb'$ ) respectively.

If we consider that each beam has a value of maximum irradiance  $I_b$ , then in absence of particles in the probe volume, the maximum irradiance measured at the detector plane would be  $2I_b$ , and 0 in the region of the shadow image of a particle placed on the centre of the probe volume. For defocused particles, the overlapping region on the detector plane is the image of the region of the probe volume which is blocked by both beams whereas the non-overlapping shadow region is the image of the area of the probe volume in which a particle blocks part of one beam but allows the other beam to freely propagate. In such a case therefore, the measured irradiance on the detector plane would be 0 (*blocked beam*) +  $I_b$  (*unblocked beam*), i.e. half the maximum value of  $2I_b$ . If we normalise those values with the maximum  $2I_b$ , which was the sum of the maximum irradiance of each of the two beams, the normalised irradiances (in the general case where a particle is defocused) correspond to the three regions of dark overlapping (“dark shadow”)<sup>8</sup>, non-overlapping shadow (“bright shadow”) and bright regions would assume values of 0, 0.5 and 1 respectively. This theoretical result has been experimentally confirmed by Hardalupas *et al.* (1994) and has the consequence that since the presence of a shadow is a binary phenomenon<sup>9</sup> the technique can be rendered amplitude-independent, provided that the value of  $2I_b$  is experimentally determined as described below.

<sup>7</sup> which coincides with the axis of optics.

<sup>8</sup> See also footnote 2. The “dark” shadow corresponds to “umbra” and the “bright” to “penumbra”. The English, descriptive terms have been preserved in this thesis in place of the Latin terms.

<sup>9</sup> The word binary refers to the fact that it is generally true that a shadow is either present or absent on the detector plane and, despite the distinction of shadows into “bright” and “dark” in the case of defocused particles, it is only necessary, during data processing, to distinguish between the binary possibility of the *presence* or *absence* of a shadow. This fact has been exploited in the design of the signal processor used in the open flame and near-burner confined flow measurements of Chapter 4 and the two-phase flow measurements of Chapter 5.

It must be mentioned here that at sufficiently large defocus distance, the two shadow images will cease to overlap and therefore no dark shadow will be observed on the detector plane. This case was not considered in the analysis of the previous paragraph because, as shown in §2.5.2, the signal processor used in most experiments was designed to ignore particle trajectories for which no dark shadow occurred.

The original assumption in the preceding description that the particle was stationary in the LDV probe volume does not affect the generality of the observations. As particles travel through the probe volume, a snapshot of the shadow image on the detector plane during particle transit would appear as described in the previous paragraph for stationary particles. Figures 2.2(a) and (b) also show idealised representations of the output signal from a photodiode that recorded the transit of the particle through the probe volume for the two *defocus* cases presented earlier. The idealised voltage output was not a function of particle diameter. For an in-focus particle,<sup>10</sup> the signal had the form of a trapezoidal wave, where the *minimum* corresponded to passage of the shadow over the detector and the *maximum* to absence of shadow. When the particle was defocused the signal also assumed an intermediate voltage level which, as explained earlier, was half the maximum and corresponded to the “bright” shadow of the particle, whilst the minimum corresponded to the “dark” shadow. The shapes of the signals presented in figure 2.2 are idealised and shallower voltage level changes were recorded by Hardalupas *et al.* (1994) in their experiments during passage of particle image over the detector, which necessitated use of experimentally-determined voltage threshold levels to distinguish between “bright” and “dark” shadows. Hardalupas *et al.* (1994) selected voltage levels of 40% and 75% of maximum, which means that any signal between 40 and 75% of maximum (*i.e.* maximum laser irradiance on the detector) corresponded to a “bright” shadow whilst smaller and larger outputs to “dark” shadow and no shadow respectively.

## 2.4 Effects of Particle Trajectory Angle

It has been assumed for simplicity of explanation that a particle and, thus, its shadow image travels normal to the array. Generally, almost no region of particle unidirectional motion exists in flows of practical interest, like swirling reacting flows and it is most likely that the condition of normality is rarely satisfied. Figure 2.3(b) illustrates how images appear in the image buffer<sup>11</sup>, when particles travel at angle  $\phi$  relative to the normal to the axis of the array, figure 2.3(a). For convenience only, it is assumed that particles were spherical. The shapes of the circular shadows have been intentionally distorted to demonstrate the effect of trajectory angle, defined on a plane normal to the plane of the beams. Provided that particles are sufficiently (see below)

---

<sup>10</sup> Particle moving across the centre of the probe volume

<sup>11</sup> This term refers to the *host computer* memory where the image of a particle is stored after sampling.

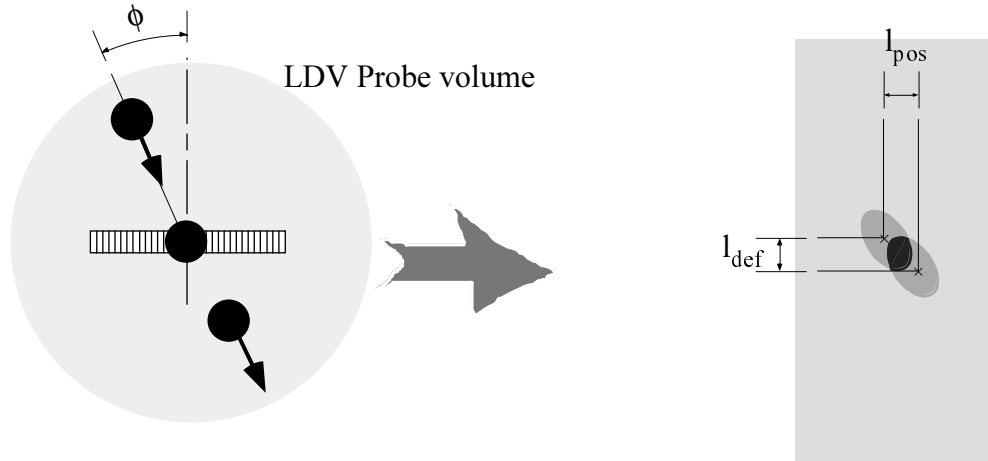


*Figure 2.3 Illustration of image appearance in image buffer: (a) Schematic of spherical particle moving at angle  $\phi$  relative to the normal to the detector and (b) image in image buffer after acquisitions of a spherical particle moving at angle  $\phi$  as in (a);  $l_{\text{def}}$  and  $l_{\text{pos}}$  denote image separation across and displacement along detector respectively. The spherical particle is moving on a plane (i.e. the plane of the paper) normal to that which contains the beams.*

defocused, the two images are displaced along and across the detector by  $l_{\text{pos}}$  and  $l_{\text{def}}$  respectively. The former is a result of the trajectory angle, whilst the latter is due to the defocus distance  $z_{\text{def}}$ . Using simple geometry, the defocus distance and the trajectory angle are deduced from the following relations:

$$z_{\text{def}} = \frac{l_{\text{def}}}{2 \tan(\vartheta)} \quad (2.1)$$

$$\phi = \tan^{-1} \left( \frac{l_{\text{pos}}}{l_{\text{def}}} \right)$$

where  $\vartheta$  is the laser beam half-angle of intersection and  $l_{\text{pos}}$  and  $l_{\text{def}}$  are measured quantities.

## 2.5 Data Acquisition and Processing

This section is divided into two subsections. The first deals with the recording of the particle shadows using the linear photodiode array and hence the custom-built processor is described and the second explains the software validation sequences applied to the raw data.

### 2.5.1 Data acquisition

According to §2.3, a particle illuminated by a laser beam casts a shadow on the detector plane which equals the size of the cross-sectional area of the particle multiplied by the magnification factor of the collection optics. Particle size can be therefore deduced from measurement of the area of the two-dimensional projected shadow image and the detector used for this purpose is described below.

The photodetector used in this work was a linear photodiode array comprising 32 elements (refer to footnote 6) 1 mm wide and 4 mm high, capable of continuously recording data at sampling rates of the order of 10 MHz. Although the shadow is a two-dimensional image, and a CCD camera seems a natural choice as detector, particular as to date CCD cameras can be gated down to a few milliseconds, which is adequate to “freeze” the moving image of the particle. However, the repeated sampling rate of common CCD cameras is limited to television frame rates of 25 Hz (and up to 50 or 60 Hz), much lower than the Kilohertz-rates required in the flows investigated in this work. In addition, the amount of data transferred to the host computer per sampling cycle in the case of the linear array is drastically smaller than the case of a CCD camera due to the larger number of elements on the latter, typically 512x512. On the other hand, use of a linear photodiode array implies that the moving shadow image must be “sliced-sampled” continuously and one-dimensional records must be used to reconstruct the two-dimensional shadow image.

The way in which one-dimensional samples were taken and their relationship to the actual two dimensional shadow image is explained in figure 2.4, which shows the passage of the shadow image of a defocused particle over a photodiode array with axis normal to the plane containing the laser beams, as in figure 2.1, and sampled continuously at fixed sampling rate. The projected Ferret diameter<sup>12</sup> of the particle under consideration was smaller than the width of the detector, because if its Ferret diameter were larger then part of the image would have been clipped (vignetted) and the particle size would have been underestimated by an indeterminable factor. According to §2.3, a defocused particle crossing the LDV probe volume cast an image on the detector which consisted of a “dark” and a “bright” shadow, appearing as shapes of different grey shades in figure 2.4. During particle passage, the array sampled only a one-dimensional slice of the moving image at each instant, and the proportion of that slice occupied by the shadow varied between samples, because the particle location had changed as a result of its velocity.<sup>13</sup> In figure 2.4 the location of an image relative to the array at three instants  $t_1$ ,  $t_2$  and  $t_3$  is presented, and it has been assumed that the particle moved with an arbitrary velocity and direction relative to the axis of the array. Provided that sampling rate was

<sup>12</sup>The Ferret diameter is defined as the maximum dimension of the particle cross-section normal to the direction of motion. The Projected Ferret diameter is the one measured on the detector plane, *i.e.* after optical magnification has been taken into account.

<sup>13</sup>It mentioned in §2.7 it was necessary that the velocity of a particle be larger than 0.5 m/s, so that its shadow image did *not* appear stationary on detector plane, as this measurement would have been rejected.

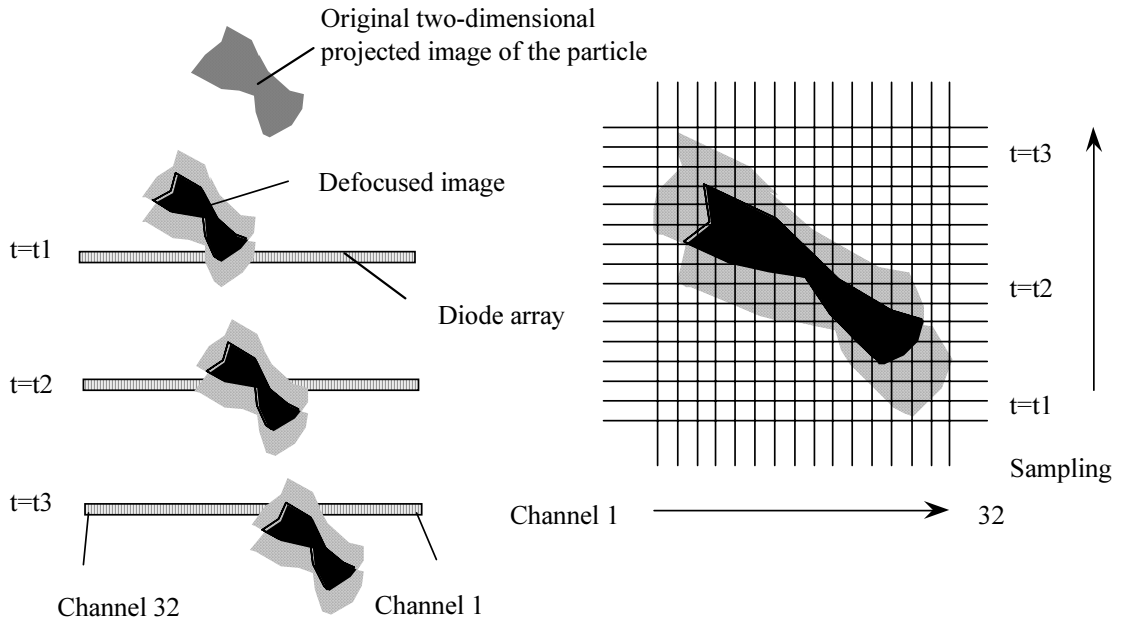


*Figure 2.4 Example of sampling and image reconstruction of the shadow image of a defocused irregular particles, showing how the sampled one-dimensional “slices” are juxtaposed to form the two-dimensional image.*

sufficiently high -sufficiency will be defined in following text- a time-series of one-dimensional slices was generated. An example of juxtaposed time series is presented in the cartesian grid of figure 2.4, where the horizontal grid corresponds to the length of the detector and each vertical grid line to the time series of the sampled output of each diode segment.

Although figure 2.4 describes the principle behind one-dimensional sampling, it does not take into account the ratio of the (finite) width of the detector and the distance normal to the array travelled by the shadow image between consecutive samples. The effect of the latter can be better illustrated in mathematical form as follows. Assume, without loss of generality, a particle travels across the SDV probe volume on the plane containing the beams and that the detector is sampled at a rate  $F$  [MHz] and a time  $\Delta t$  has lapsed between consecutive samples:

$$\Delta t = \frac{1}{F} 10^{-6} [\text{s}] \quad (2.2)$$

If the velocity component of the particle normal to the fringes were  $U_{\perp}$ , then the distance travelled by the particle in the SDV probe volume in that direction during time  $\Delta t$  would be:

$$\Delta \ell = U_{\perp} \cdot \Delta t [\text{m}] \quad (2.3)$$

and therefore, the shadow image of the particle would have travelled a distance  $\Delta L$  in the image (i.e. detector) plane during time  $\Delta t$  over the detector distance:

$$\Delta L = G \cdot \Delta \ell \text{ [m]} \quad (2.4)$$

where  $G$  was the magnification factor of the collection optics and all quoted distances are in meters. Combining equations (2.2)-(2.4) it is concluded that between successive one-dimensional slices a particle shadow image has moved over the detector by:

$$\Delta L = G \cdot U_{\perp} \cdot \frac{1}{F} \text{ [\mu m]} \quad (2.5)$$

A consequence of equation (2.5) is that the distance travelled by the shadow image between samples was inversely proportional to the sampling rate and, for example, doubling of the sampling rate resulted in halving of the distance travelled by the shadow for given particle velocity.

Assume for simplicity that the particles are spherical of diameter  $d$ , and that their velocity vector is normal to the axis of the linear array. The size of the shadow image of such particle in the detector plane is:

$$L = G \cdot d \quad (2.6)$$

Division of equation (2.6) by (2.5) results in the following formula which gives the number of samples necessary to sample the whole shadow of a moving spherical particle of diameter  $d$  travelling with velocity  $U_{\perp}$ , when the sampling rate is  $F$ :

$$N = \frac{L}{\Delta L} = \frac{F \cdot d}{U_{\perp}} \quad (2.7)$$

In figure 2.4,  $N$  is the number of horizontal grid lines which *contain* part of the shadow of the particle. In the case of irregular particles the same principle applies, but the distance travelled by the shadow image across the detector depends on the orientation of the particle, since the particle aspect ratio is not necessarily one as, for example, is the case for the particle of figure 2.4.

Equation (2.7) shows that the number of samples taken during particle passage is proportional to the sampling rate. If the sampling rate is small and the numerator of equation (2.7) equals the denominator, then only *one* sample is taken during particle passage. This way, particle shape in the direction normal to the axis of the array (and, hence, size) would not be resolved from just one one-dimensional slice. On the other hand, if sampling rate is sufficiently large the number of samples will be adequate to reconstruct the shape of a particle in the direction normal to the axis of the array. Between these extremes an *optimum* exists (see below) and is defined as the number of samples obtained at a sampling rate such that the distance travelled by the shadow *image* over the linear array (*i.e.* in the detector plane) between successive samples is equal to the diode pitch, 1 mm for the photodiode array used in this work. The optimum is thus defined as the sampling rate at which the resolution of the sampled shadow imaged in the direction normal to the array is equal to that along the axis of the array.<sup>14</sup> On the assumption that a spherical particle of diameter  $d$  and velocity  $U_{\perp}$  is sampled, the number of samples taken under the optimum condition is:

$$N = \frac{10^3 \cdot d}{U_{\perp}} \quad (2.8)$$

where  $d$  is in [ $\mu\text{m}$ ] and  $U_{\perp}$  in [ $\text{m/s}$ ]. Substitution of the value of  $N$  from equation (2.8) into equation (2.7) yields the appropriate sampling rate. Use of the sampling rate estimated according to this condition implies that enough samples were taken to ensure that the particle dimension which corresponded to the direction normal to the array (along a vertical grid line in figure 2.4) was resolved with precision no worse to that of the dimension parallel to the array axis. Accordingly the cells in figure 2.4 have been depicted as squares and if all one-dimensional slices were placed next to each other in the manner of figure 2.4, the sampled circular shadow image would appear circular overall (with castellated perimeter). It must be noted at this point that the assumption of spherical particles does not impose restrictions on the analysis and was made only for simplicity.

In general, particles travel with a distribution of velocities whilst the sampling rate of the electronics is fixed<sup>15</sup>, and the number of samples taken is different from the calculated optimum. Figure 2.5 presents examples of the reconstructed image of a spherical particle from samples made at rates higher and lower than optimum, termed *oversampled* and *undersampled* respectively. In drawing the reconstructed images it has been assumed that the particle velocity was such that the raw shadow image moved across the detector and normal to its axis by 1 mm (the diode pitch) *between successive samples*. The reconstructed shadow image of an oversampled spherical particle appears longer than the raw whilst an undersampled image appears shorter,

<sup>14</sup> According to this statement, if the sampling rate is higher than the optimum the image resolution in the direction normal to the axis of the array will be higher than that along the axis of the array; this, though, would not result in higher precision of sampling of the entire image (which is limited by the *worst* resolution, *i.e.* the resolution along the axis of the detector) and, thus, would not be an optimum sampling rate.

<sup>15</sup> Which is indeed the case with the signal processor.

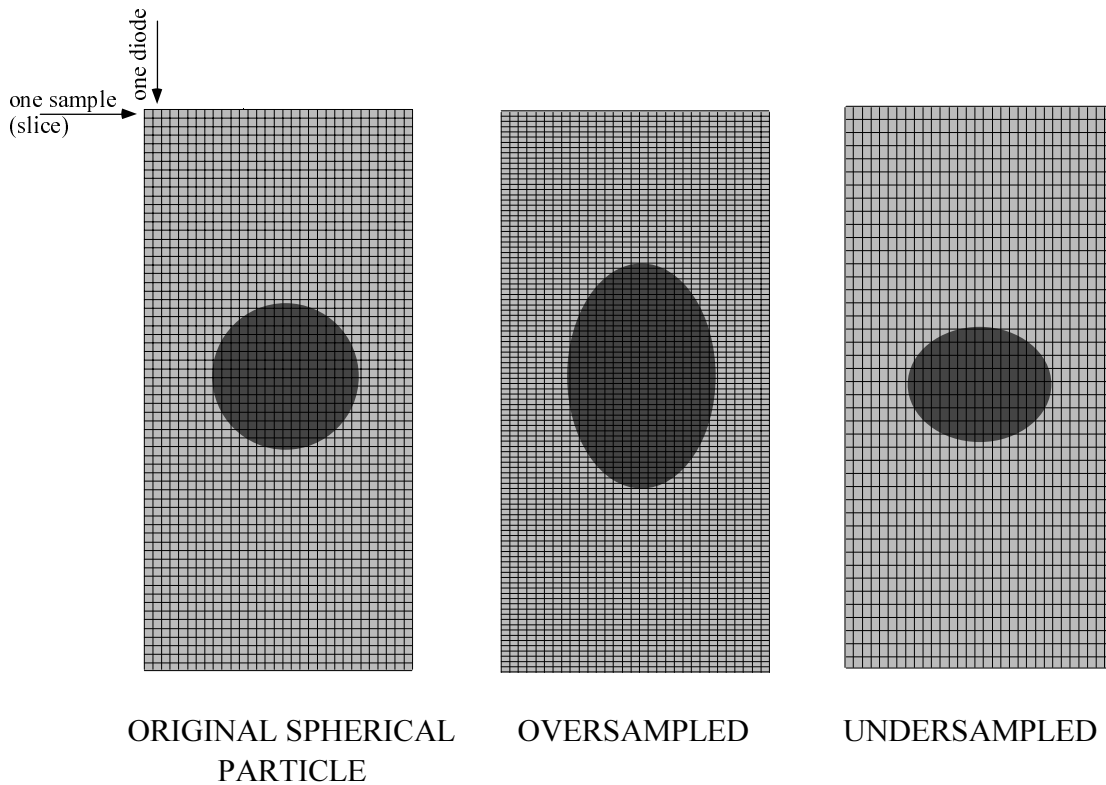


*Figure 2.5 Examples of the reconstructed recorded shadow image of a spherical particle in the image buffer showing the effects of over- and undersampling.*

because the raw image translation over the array was smaller and larger, respectively, than assumed during reconstruction of these shadows. The calculated aspect ratio of the reconstructed image would generally be different from that of the raw shadow image on the detector plane (before corrections in software are applied, see §2.5.4) as a consequence of a combination of particle velocity and sampling rate different to the corresponding optimum from equation (2.8) assumed in drawing the images. The reader should refer to §2.5.4 below, where equation (2.9) presents mathematically how oversampling and undersampling occur (and how they are corrected in software).

Hence, the question arises is as to the correspondence between the reconstructed image (formed if all of one-dimensional slices were placed next to each other in the manner of figures 2.4 and 2.5) and a snapshot of the raw moving shadow image (*e.g.* photographed by a camera on the detector plane). Image distortion due to under- or oversampling is alleviated by simultaneous measurement of the velocity of a particle which can be introduced in the system of equations (2.2)-(2.7) and be applied to correct the aforementioned under- or oversampled image. The details of the correction sequence applied during reconstruction of the actual images from the sampled data are described in §2.5.4.

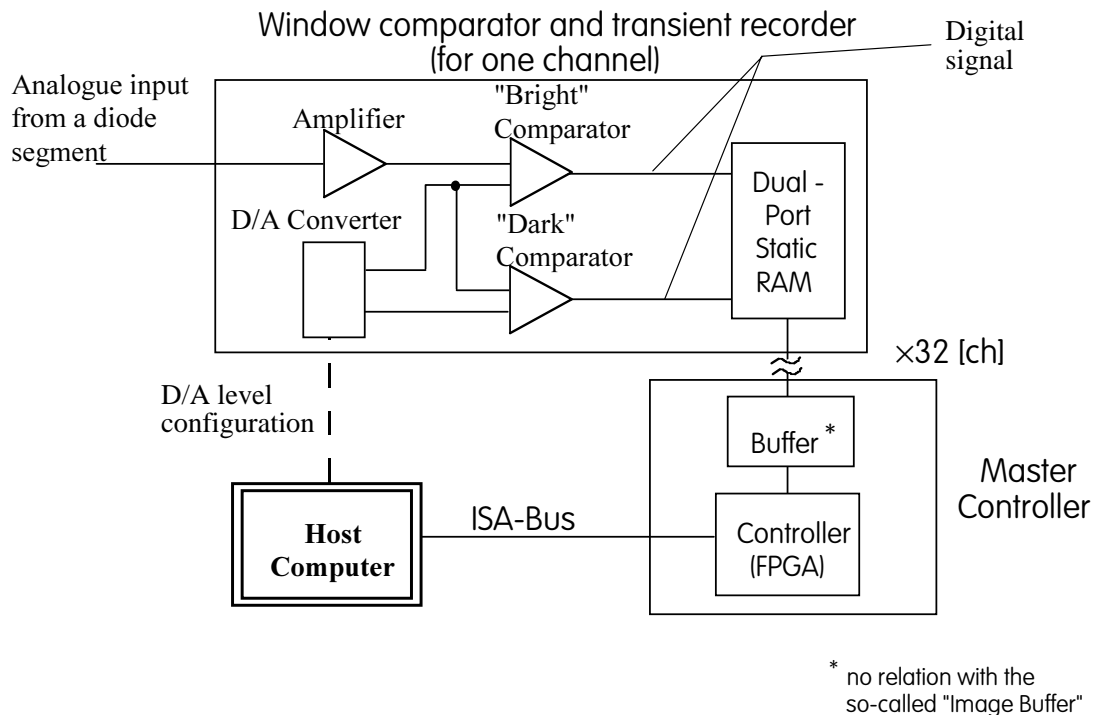


*Figure 2.6 Block diagram of the SDV signal processor showing the components for processing the analogue output signal from one diode of the array. The electronic component defined as FPGA is the programmable integrated circuit which controls the hardware.*

### 2.5.2 Signal processor

The requirement from the signal processor of the SDV signals was to sample the output signal of each diode segment and transfer the data to the host computer for processing which would include recognition of areas corresponding to "dark" and "bright" shadows, and to no shadows at all. The processor used by Hardalupas *et al.* (1994) and Morikita *et al.* (1995) was based on A/D conversion of the output of each diode and software processing of the converted signals. This method permitted simple electronic circuitry based on 8 bit A/D converters but resulted in large amounts of data being transferred to the computer with consequent low particle image acquisition rates which were inadequate for particle flux and volume fraction measurements. The design was later improved and all measurements in this thesis, except those at the downstream region of the confined flow in Chapter 4, were measured with the signal processor described below.

In order to make flux and volume fraction measurements feasible, the speed of the processor was increased from the configuration used by Morikita *et al.* (1995) and the amount of data transferred to the host computer was reduced by adopting a different method of processing. A new data recorder was developed, consisting of 2-bit analogue window comparators and digital

transient recorder, shown in figure 2.6. The window comparators were aligned to distinguish three different irradiance levels, two of which corresponded to the “dark” and “bright” shadows, and the third to the absence of shadow on the detector. The threshold levels of the comparators were set empirically at 75 and 40% of the maximum amplitude (Hardalupas *et al.* 1994): the maximum amplitude corresponded to irradiance levels on the detector in the absence of particles in the probe volume, and the two threshold levels were used to discriminate between dark shadows (irradiance levels smaller than 40% of maximum<sup>16</sup>) and bright shadows (between 40 and 75%).<sup>17</sup> The output signal of each comparator (*i.e.* the comparators for the “bright” and the “dark” shadows) were passed through a “latch”, the purpose of which was to combine together the digital outputs of the comparators and synchronise them with the clock of the SDV processor.<sup>18</sup>

This arrangement allowed faster, hardware processing of the images, performed by the comparators rather than software processing of the A/D converted signals, and also the amount of the digital data transferred to the host computer was reduced by 75% compared to the 8 bit A/D converted signals.<sup>19</sup> In addition, the data transfer rate from the processor to the host computer was increased by a factor of 10 compared to all previous work<sup>20</sup> and, hence, the maximum measurable particle number density was further increased.

The processor was designed to be triggered only by “dark” shadows -thus only by particles at small defocus distances- as this kept the sizing uncertainty to less than 10% (Hardalupas *et al.* 1994). The processor had two independent sets of memory (dual-port static Random Access Memory), with 4096 samples/channel for 32 channels for storage of the signals from the comparators. The reason for two sets of memory is that when the SDV stores the processed

<sup>16</sup>The maximum was measured in the absence of particles and this ‘referencing’ procedure allowed estimation of the signal output corresponding to irradiance  $2I_b$  mentioned in §2.3. The reference voltage served to normalise signals and thus, allowed distinction between various types of shadows as explained. The ‘referencing’ procedure was performed at the beginning of each experiment or whenever irradiance on the photodetector decreased as, for example, the case of beam extinction through soiled windows in confined measurements.

<sup>17</sup>The digital threshold levels of the comparators were set by the D/A converters. The full analogue scale (output of each segment of the linear array) corresponding to voltage scale between “dark” shadow and absence of shadow was divided by 256 (8-bit D/A,  $2^8=256$ ) and the digital levels corresponding to 40% and 75% threshold levels were set by the D/A converters for subsequent use by the comparators.

<sup>18</sup>The 2-bit digital output of the latch was either “00” (irradiance levels below 40%, *i.e.* “dark” shadow), “01” (irradiance levels between 40% and 75%, *i.e.* “bright” shadow) and “11” (irradiance levels above 75%, *i.e.* no shadow). Output “10”, which would have meant that irradiance levels were below 40% *and* above 75% is, of course, not possible.

<sup>19</sup>Since images were digitally stored, a record from each diode at any instant that could be either covered by a shadow or not, could be represented by a binary digit, assuming values of 0 (no shadow) and 1 (shadow). The advantage was smaller storage space and higher processing speed.

<sup>20</sup>Instead of using an interface card which performs DMA transfers from peripheral devices attached to the computer to the main computer memory, the current SDV processor was connected to the computer *directly* on the computer ISA bus. This way, the memory in the SDV processor was attached to the main computer memory and was “seen” by the computer as extended memory. The computer was then able to perform transfers between the “peripheral” (SDV) memory and its main memory at rates about 10 times faster than through DMA. This design allows increasingly faster data transfers between peripherals (such as the SDV processor) and computers as the computer system buses become faster. One, for example, can design an interface card which will utilise the PCI bus of modern personal computers and achieve data transfers more than an order of magnitude faster than those quoted in Table 2.1.

signal from the linear array in one set of memory, the contents of the other memory set can be transferred to the main computer memory. Upon completion of this storing/transfer procedure of the SDV processor, the two memory sets can be swapped and this procedure can be re-initiated. This design minimises the idle time of the processor and maximises the acquisition rate of the instrument. The operation of the SDV processor was based on pretrigger recording, to allow capturing of the part of the image which preceded the trigger event. The processor sampled continuously (and stored the processed signal in the one set of memory) and if a trigger event occurred, the storing/transfer procedure mentioned above was initiated, upon completion of sampling of a predefined number of samples.

**Table 2.1: Specifications of the SDV signal processor**

Input Channels	32 (can be extended up to 128)
Sampling Frequency for Shadow [MHz]	10
Sampling Frequency for LDV [MHz] <sup>1</sup>	10
Data transfer rate [Mbytes/s]	2.0
Interface	IBM-PC/AT (ISA)

The detailed specifications of the processor are listed in Table 2.1. The maximum data rate of the present hardware was about 300 particles per second and was limited by the data transfer (the capability of the ISA bus) to the host computer rather than by the sampling rate. The sampling frequencies for the LDV processor and for the shadow are limited by the design of the current circuitry.

### **2.5.3 Simultaneous size and velocity measurement**

The requirement to measure particle velocity simultaneously with size necessitated synchronisation of the velocity and size signals and processing of the Doppler signal by a zero-crossings counter<sup>22</sup>. The synchronisation was achieved by monitoring the output of the central diode of the array and the Doppler signal and adjusting the alignment of the photomultiplier

<sup>21</sup> Although the processor has built-in A/D converters for sampling Doppler signals, the maximum sampling frequency of 10 MHz of the present electronics was considered inadequate to resolve the Doppler frequencies of velocities encountered in the near-burner region of the swirl burners examined in this thesis. An arrangement with a zero-crossings counter, described in the following section, was preferred. Nevertheless, in the water channel flow used for the estimation of accuracy of flux measurement of §2.6.4, the flow velocity was about 4 m/s which, for the optical setup of that experiment, could be resolved by FFT of the signal sampled at 10 MHz.

<sup>22</sup> In the measurements in the far-burner confined flow of Chapter 4 a FFT processor was utilised instead of a zero-crossings counter, because of unavailability of the counter at that time. Synchronisation was achieved by monitoring the trigger pulse which was the same for both (SDV and Doppler) signals.

<sup>23</sup> The number and location of trigger diodes is set by the operator of the instrument.

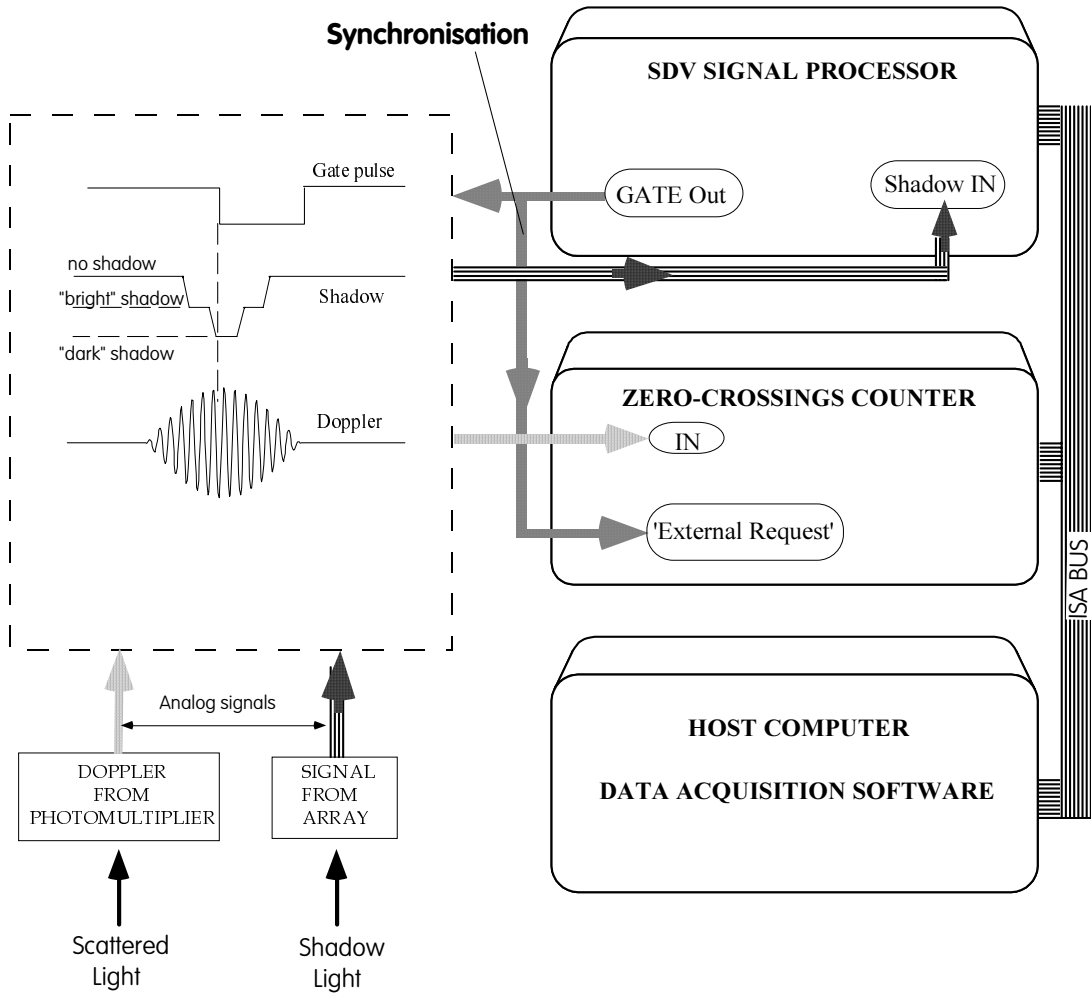


Figure 2.7 Block diagram of the electronics for simultaneous size and velocity measurement using SDV indicating the connections between the SDV signal processor and the zero-crossings counter to the host computer.

until the maximum of the Doppler- coincided with the minimum of the shadow signal. Figure 2.7 presents block diagram of the electronic arrangement which ensured simultaneity between size- and velocity data acquisition. The trigger event was provided by the SDV processor which issued a TTL pulse upon detection of a “dark” shadow by a number of trigger diodes (arbitrarily set to eight or ten in this work) symmetrically located in the centre of the array<sup>23</sup>. The TTL pulse was fed into a 20 MHz Wavetek function generator (Model 145, Wavetek Corp.)<sup>24</sup> which produced a variable-width TTL gate pulse that was connected to the ‘external request’ input of the custom-built phase Doppler zero-crossings counter (so-called Model 1), operating in single-channel mode. Hence, the counter was only processing input Doppler

<sup>24</sup> The function generator was later replaced by custom-built electronic circuitry placed inside the SDV processor to reduce the complexity of connections.

signals, high-passed at 1.5 MHz, while the ‘external request’ input was fed with the gate pulse. The width of the gate pulse was previously adjusted by trial-and-error procedure that maximised the data rate during measurements in the regions of reverse flow velocity of the burner of Chapter 4, so that no velocity measurements were rejected because of an inadequate number of detected zero-crossings during gating.<sup>25</sup>

#### 2.5.4 Validation sequence of SDV raw data

Once data were transferred from the SDV processor to the computer memory, a sequence of validation criteria were applied to the raw signals with the purpose of extracting validated shadow images and calculating their area, from which a characteristic particle diameter was defined, as described later in this section. The steps followed until a valid shadow image was extracted from the one-dimensional sampled slices were the following:

##### Validation of Velocity Signal

The validation procedure continued provided that particle velocity was valid (see §2.5.1). On invalid velocity, the current shadow measurement was abandoned and sampling was re-initialised with the next particle.

##### Creation of an Image Buffer for Storing the Sampled Images

A number of 1024 photodiode voltage samples were taken, on average, per particle measurement, at sampling rates  $F$  [kHz] varied between 1250 and 5000 kHz in the present experiments. The sampling rates were empirically selected to satisfy the “optimum” criterion explained in §2.5.1 (and mathematically described by equation 2.9). As shown earlier in equation (2.5), the distance travelled by the shadow image across the detector between successive samples depended on particle velocity and was thus different from the diode pitch. This distance was:

$$r = \frac{1[\text{mm}] \cdot F[\text{kHz}]}{U_{\perp} [\text{m/s}]} \quad [\text{no units}] \quad (2.9)$$

In this equation 1 mm is the diode pitch and  $U_{\perp}$  the particle velocity normal to the axis of the photodiode array, measured simultaneously with the sampling of the shadow image. Variable  $r$  gives the distance travelled by the shadow measured in units diode pitches and, for example,

<sup>25</sup> Phase Doppler counter model 1 of the Thermofluids Section at Imperial College was design to accept only those signals for which a minimum of 9 zero-crossings were detected. Detailed description of the hardware- and software validation procedures is beyond the scope of this thesis and the reader should refer to Hardalupas and Laker (1993).

$r=0.5$  means that between samples the shadow image moved by  $1 \text{ mm} / r$ , *i.e.*  $2 \text{ mm}$  across the detector and, therefore, the image was *undersampled*. In case of  $r=1$  then the sampling rate was optimum according to definitions of §2.5.1. The calculated value for  $r$  was used to correct the image for *under-* or *oversampling* and restore the correct aspect ratio which was distorted due to sampling rate unequal to the optimum. The correction was performed by scaling the distance between two horizontal gridlines of figure 2.4, using the value of  $1/r$ , to be equal to  $1 \text{ mm}$  (the diode pitch), so that the cells of figure 2.4 are square (which is not the case before correction, figure 2.5).

The corrected image was stored in an image buffer for further processing.<sup>26</sup> Because the image has been corrected with parameter  $r$ , all lengths are henceforth quoted as multiples of *diode pitch*. The size of the image buffer was  $32 \times 96$ <sup>27</sup> (diode pitches<sup>28</sup>), thus a *maximum time record from sampling the shadows, which was equivalent to three-times the width of the array* was allowed for storing the image. In other words, the longest particle dimension across the detector could not exceed  $96 \text{ mm} / (\text{magnification ratio})$ . The size of the image buffer was selected to maximise the data and processing rate and was sufficient for most particles encountered in practical reacting two-phase flows; only in the case of long fibres, for example, could it have proven inadequate.<sup>29</sup>

### Separation of Raw Images and Cross-Correlation

Once the image buffer, which consisted of the sampled one-dimensional slices (the image buffer can be visualised as the grid of figure 2.4), was created multiple scatterer events were removed, by identifying a contiguous area of “bright” and “dark” shadows, surrounding the one-dimensional slice which corresponded to the trigger event.

In the general case, single particles cast two “bright” shadow images on the detector which overlapped in part, forming a “dark” shadow.<sup>30</sup> The purpose of the separation was to distinguish the two shadows originating from each laser beam and be able subsequently to perform a cross-correlation between them. The procedure for division of the image and separation into

<sup>26</sup> Before correction an image in memory would occupy, for example,  $32 \times 1024$ , if 1024 were the number of samples per particle. Obviously a lot of memory is inevitably consumed when a particle is small and moves fast, but the number of samples is so selected as to enable complete sampling of particles of different diameters and velocity.

<sup>27</sup> Fixed in software in the current SDV design and by no means a limiting feature of the instrument. This selection resulted from optimization between speed of processing and ability to sample the coal particles of the present work which are unlikely to have aspect ratios larger than 3 (96:32).

<sup>28</sup> Literally *bits*, but each bit had an equivalent length (in world units) of 1 diode pitch (=1 mm). Binary arithmetic was used in the storing and processing of the shadow images that allowed faster data acquisition rates than if integer arithmetic were used.

<sup>29</sup> As shown in §2.7, the same applied for the case of particles travelling with velocities smaller than about  $0.5 \text{ m/s}$ .

<sup>30</sup> It is recalled that if defocus was large enough and no overlapping occurred the SDV signal processor would *not* be triggered.

<sup>31</sup> Although it may not be clear to the reader, performing a “cut” was the computationally fastest method for separating the images.

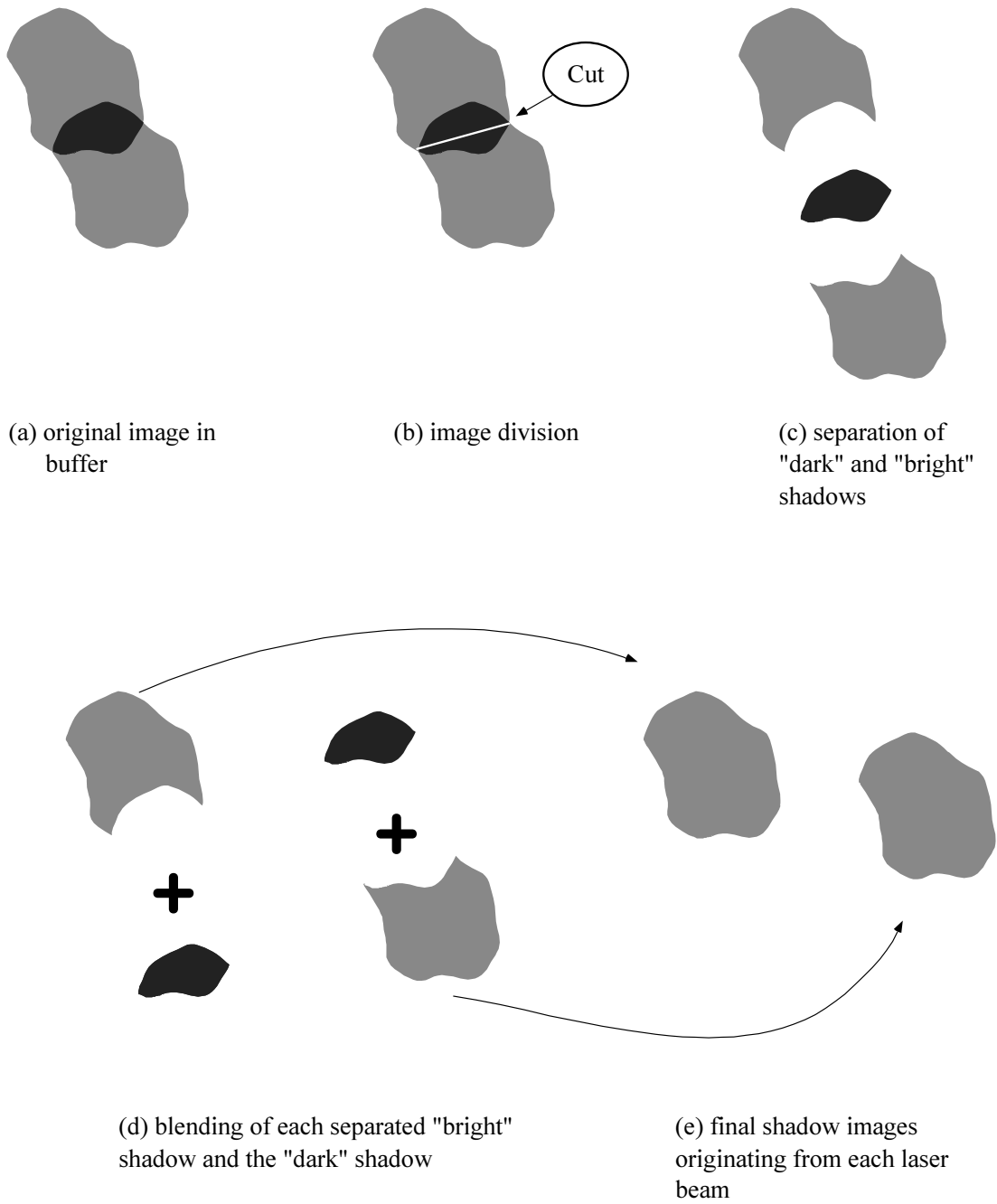


*Figure 2.8 Schematic of the algorithm for separation of the two overlapping images, originating from each incident laser beam, in the image buffer. The (a) original image in the buffer is (b) divided in two by cutting across the boundary image intersection points; the "bright" shadow from each beam is (c) distinguished from the "dark" after division and (d) each "bright" shadow is blended with a copy of the "dark" shadow to form (e) the actual shadow image of the particle originating from each laser beam.*

two shadows is illustrated in figure 2.8. The original image (a) containing "dark" and "bright" regions which were digitally stored and therefore their boundaries were sharp and directly distinguishable, was separated in (b) by a cut through the weighted centre of the dark shadow<sup>31</sup>, and (c) the area that corresponded to "dark" shadow was removed, resulting in three parts

constituting the original image which were (d) recombined into pairs of “bright” shadow/”dark” shadow images to result in (e) two distinct images originating from each laser beam.

After division, the images were bitwise cross-correlated to determine whether they were actually shadows of the same particle illuminated by two laser beams, rather than the result of noise. Additional information obtained by cross-correlation were the displacements  $l_{\text{pos}}$  and  $l_{\text{def}}$  in figure 2.3, which were related to the particle trajectory angle and defocus distance, respectively, according to equation (2.1). The resolution of calculation of  $l_{\text{pos}}$  was equal to the diode pitch of the image of the array in the sampling space (*i.e.* 1 [mm]/ magnification ratio), whereas for the  $l_{\text{def}}$  it was  $\Delta z$ , according to:

$$\Delta z = \frac{1[\text{mm}]/G}{2 \tan(\vartheta)} \quad (2.10)$$

The value of the latter is order-of-magnitude higher than that of the former and would yield to unacceptable random uncertainty in calculation of the trajectory angle. In order to improve the accuracy of the calculation, an interpolating technique, based on the “adjusted Gaussian fitting” procedure (Kobashi *et al.* 1990) was used to provide better accuracy for the measurement of the defocus distance and, thus, the trajectory angle.

Estimation of the trajectory angle required a minimum defocus equal to  $\Delta z$  (*i.e.* the minimum resolvable defocus distance), otherwise with zero defocus equation (2.1) became indefinite. The trajectory angle was estimated with higher accuracy as the defocus distance increased, due to the resolution defined by equation (2.10), but a ceiling was placed on the defocus distance equal to 500  $\mu\text{m}$ , because according to Hardalupas *et al.* (1994) sizing errors higher than 10% in higher defocus distances were the result of deterioration of image quality, caused by the finite depth-of-focus of the receiving optics. This defocus limitation was applied by software in the post-processing of the measurements and was independent of data acquisition.

### Estimation of the Area of the Shadow Image

Two independent calculations were performed. The first was based on calculation of the number of diodes in the image buffer covered by a shadow. If we denote by  $S_U$  the area covered by a “dark” shadow and by  $S_L$  that by a “bright” one, then the average area,  $S_P$ , covered by the shadow from one beam (see figure 2.9, for example) is:

$$S_P = \frac{2S_L + S_U}{2} \quad (2.11)$$

A common parameter defined to characterise the size of a non-spherical particle is the diameter of a spherical particle with the same cross-sectional area (*e.g.* Morikita *et al.* 1995; Orfanoudakis and Taylor 1995), particularly when measuring by (diffracted light) amplitude-based techniques (as in the work of Orfanoudakis 1994), which has been followed here. Hence, the diameter of spherical particle with the same cross-sectional area as the area of the measured shadow is

$$d_p = \sqrt{\frac{4}{\pi} S_p} \quad (2.12)$$

The second method for the estimation of  $S_p$  was based on cross-correlation and was used for cross-checking and identification of images from multiple-scattering. The area was determined by measuring the area common to both shadow images, once they were shifted until they overlapped in the image buffer; shifting was performed until the cross-correlation was maximised.

Areas calculated by both methods were subsequently compared and the measurement was rejected if the area difference was larger than 50%, an empirically-determined limit (Morikita 1996). The latter criterion allowed images due to multiple scattering to be rejected.

## 2.6 Accuracy of Particle Flux and Volume Fraction Measurement

### 2.6.1 Introduction

The measurement of flux and volume fraction of a dispersed phase represents an outstanding difficulty for optical single particle counters. For both cases of spherical and irregular particles, which are typically measured by phase Doppler anemometry (PDA) and diffracted light amplitude (*e.g.* Hirleman *et al.* 1982; Morikita *et al.* 1994; Orfanoudakis and Taylor 1992 & 1995; Yeoman *et al.* 1982) respectively, the determination of the local particle flux or concentration is associated with substantially higher uncertainties than is the case for the size and the velocity. This is because flux and concentration are not directly measured, but calculated from the particle velocity and size and a corresponding cross-sectional area, or volume, of the optical probe volume. It is the uncertainty in the latter two quantities, and particularly their dependence on particle size due to the Gaussian irradiance of the incident laser beams, which are the major contributors to the uncertainties (see Taylor 1995, for example, for a review of the definition of flux and concentration of a dispersed phase measured by optical methods).

In the case of amplitude-based techniques which use diffracted light, the sizing error due to the shape of the particles is typically 20% and can be as high as 70% for 20  $\mu\text{m}$  ellipsoids of aspect ratio of 2.0 (Hardalupas *et al.* 1995). There is little recent published work on flux measurements by such a technique with the exception of Orfanoudakis (1994), who used the work by Hardalupas and Taylor (1989), as developed for phase Doppler anemometry (PDA). The accuracy of flux measurement with methods as that of Orfanoudakis is expected to be similar to that for PDA, discussed below. In PDA, the size (*i.e.* area) of the optical probe volume is preferably determined *in-situ* from each measurement (*e.g.* Saffman 1987; Hardalupas and Taylor 1989; Schöne *et al.*, 1994). The extensive experience in the use of PDA has proven that the uncertainties are usually of the order of several tens of percent (*e.g.* Hardalupas *et al.* 1994b; Maeda *et al.* 1996), although these may be as low as 5% under ideal conditions (Qiu & Sommerfeld 1992; Sommerfeld & Qiu 1995). Theoretical investigations show, in addition, that the so-called “trajectory ambiguity effect” (Gréhan *et al.* 1992), also due to the Gaussian irradiance, and the so-called ‘slit effect’ (Xu and Tropea 1994) can result in an effective probe volume different from that estimated by the formulae of, for example, Saffman (1987), and this error source is a large potential contributor to the observed discrepancies. In addition, determination of the probe volume dimensions can be erroneous in the case of measurement of a two-dimensional flow using a single-channel PDA, because in the latter case the usual formula applied for the size of the probe volume assumes that the flow is always normal to the fringes (Saffman 1987).

Due to the fact that diffracted amplitude-based size measurement of irregular particles is less straightforward and accurate than for spherical ones, the imaging technique developed and described in this thesis is valuable. The sizing accuracy of the shadow Doppler velocimeter (SDV) instrument has been evaluated by comparison with microscope measurements and it was found that the sizing accuracy was better than 10% with a further  $\pm 5\%$  inaccuracy caused by so-called “defocusing” of the particle from the focal plane of the receiving optics by up to  $\pm 500 \mu\text{m}$  (Hardalupas *et al.* 1994). The instrument was later improved (Morikita 1995) by reducing the response time of the photodiode array and by increasing the number of active segments of the detector, thereby increasing the maximum measurable particle velocity and the particle size dynamic range, respectively. These features of the technique were exploited to measure the location of the particle during its trajectory through the probe volume and to measure the angles of particle trajectories relative to the axis of the photodiode array (Morikita *et al.* 1995). Additionally, the accuracy of size measurement made by this improved version was assessed in the case where the beams had to pass through optical windows and through the variable refractive index fields produced by flames, situations where amplitude-based instruments can yield unacceptably large sizing errors due to the uncontrollable thermal movement of the windows. Hishida *et al.* (1995) found that the sizing uncertainties do not exceed -12% in the former case and 15% in the latter. In this thesis (Chapter 5) it is also demonstrated that the instrument can measure the two-dimensional motion of *burning* coal

particles near the exit of an asymmetrical laboratory-scale confined coal combustor, although no particle flux or concentration is reported from this flow.

For particle mass flux and concentration measurement using SDV, the size of the effective probe volume (hereafter termed as “sampling-space” to indicate that it is explicitly user-delimited, rather than set by a combination the Gaussian irradiance profile and electronic trigger levels, with the resulting sampling-space size dependence estimated from on-line measurement, as in the case of PDA) must be accurately defined. However, the procedure of determining the sampling-space suggested by Morikita *et al.* (1995), mathematically described below by equations (2.17)-(2.20), is complicated for non-spherical particles in omni-directional flows due to the dependence of the sampling-space size on the particle size, shape, orientation and trajectory, which could cause a systematic bias in the validation rate, especially for trajectories near the edge of the sampling-space. In addition, the design of the signal processor they used implies increasing probability for particles to trigger the instrument with increasing particle size because they used a single diode as a trigger-channel. Although correction for this bias *was* included in the post-processing of their data, it is not a practically convenient design for the measurement of polydisperse particles. Therefore simplifications in the procedure for the calculation of particle mass flux and concentration are required and should be tested experimentally in order to enable accurate flux and concentration measurements in complex flows.

The purpose of §2.6 is to suggest improvements on the procedure for the calculation of the size of the sampling-space of the SDV and, using this procedure, to assess the accuracy of the flux and volume fraction measurement in a unidirectional turbulent channel water flow. Monodisperse spheres with density similar to that of water were used in the experiment, and the measurement accuracy was tested as a function of particle volume fraction. The procedure to determine the size of the sampling-space was simplified relative to Morikita *et al.* (1995) by providing a *user-defined* spatial limitation to eliminate the effect of the particle size, shape, orientation and particularly trajectory angle. As explained in §2.5.2, the signal processor was redesigned to achieve high data acquisition rates and, hence, allow measurement of particle flux and concentration in the flow.

### **2.6.2 Method of flux and volume fraction measurement**

The *mean* mass flux of particulate phase,  $G_{\perp}$  [ $\text{kg m}^{-2}\text{s}^{-1}$ ], a vector defined in the direction normal to the interference fringes in the LDV probe volume, is given by the amount of particle mass crossing unit area per unit time (Hardalupas *et al.* 1994b):

$$G_{\perp} = \frac{\rho_p}{T_s} \sum_i \left[ \frac{V(i)}{A_{\perp}(i)} \sum_{j=1}^{n(i)} \frac{u_{\perp}(i,j)}{|u_{\perp}(i,j)|} \right] \quad (2.13)$$

where  $T_s$  is the total sampling time of the measurement,  $\rho_p$  is particle density,  $V(i)$  is volume of the particle,  $u_{\perp}(i,j)$  is velocity of particle sample number  $j$  in size class  $i$ ,  $n(i)$  is the total number of particles in size class  $i$  and  $A_{\perp}(i)$  is the area of sampling-space through which particles flow with unit normal perpendicular to the fringes. The cross-sectional area  $A_{\perp}(i)$  is a function of the particle size and the method for its calculation will be described in §2.6.3. The particle volume  $V(i)$  in the case of irregular particles can be estimated only from the projected area equivalent diameter,  $d_p$ ; however, spherical particles have been used in the present study to avoid this additional uncertainty in the calculation of particulate volume fraction.

There are two different methods to determine the mean particle volume fraction with LDV-based techniques. The first, using the LDV measured particle velocity perpendicular to the plane of the fringes,  $U_{\perp}$ , assumes predominantly unidirectional flow normal to the plane of the fringes from which the particle volume fraction  $C_v(i)$  is obtained as follows

$$C_v(i) = \frac{1}{T_s} \sum_i \frac{V(i)}{A_{\perp}(i) |U_{\perp}(i)|} \quad (2.14)$$

where  $U_{\perp}(i)$  is the ensemble-averaged velocity for size class  $i$ ,

$$|U_{\perp}(i)| = \frac{n(i)}{\sum_j |u_{\perp}(i,j)|^{-1}} \quad (2.15)$$

where  $u_{\perp}(i,j)$  is velocity of particle  $j$  in size class  $i$  and  $n(i)$  is the total number of particles in size class  $i$ , measured over  $T_s$ .

This is an approximation which can yield indefinitely large errors in recirculating flows near a stagnation point, because the denominator in equation (2.14) there approaches zero. Hardalupas and Taylor (1989), based on the suggestion of Capp (1983), proposed an alternative method to overcome this problem. This method uses the residence time of a particle in the sampling-space:

$$C_v(i) = \sum_i \left[ \frac{\sum_{j=1}^{n(i)} \tau(i,j)}{T_s \cdot V_s(i)} \right] \quad (2.16)$$

where  $V_s(i)$  is the volume of the sampling-space for particles in size class  $i$  and  $\tau(i,j)$  is the particle residence time of the  $j^{\text{th}}$  particle of this size class in the sampling space.

The definition in equation (2.16) is, in principle, a better estimation of the volume fraction than equation (2.14), because it represents the duration of particle occupancy in the probe volume, which is equivalent to volume fraction independent of the velocity direction. However, if the flow is predominantly one-directional, the former equation *is* equivalent to the latter. Since the present measurements were made in a uni-directional flow, the former method was preferred. An extension of the residence time method suitable for SDV measurements is proposed in §2.6.5.

### 2.6.3 Size of the sampling-space of SDV

To measure the correct size distribution, Morikita *et al.* (1995) proposed a procedure to correct the biasing caused by the dependence of the size of the *sampling-space* inside the probe volume on particle size and defocus. The sampling-space is defined as that region of space over which a particle generated two superimposed shadows, the overlapping region of which, over some part of its trajectory, passes over the trigger diodes and which is not vignetted by the finite width of the linear array. These statements are quantified below but Morikita *et al.* (1995) showed that the sampling-space has, in principle, elliptical shape in the  $y$ - $z$  plane (figure 2.9). Their definition was, however, appropriate only for *spherical* particles travelling *normally* to the axis of the diode array when *only one* trigger channel of the diode array was used.

The equations proposed by Morikita *et al.* (1995) for the dependence of the width of the elliptical sampling-space on particle size, assuming spherical particles, are here extended to include the effects of multiple (eight contiguous<sup>32</sup>) trigger channels, of the width of the sampling-space as a function of the defocus distance  $z_{\text{def}}$ , the particle diameter  $d_p$ , the laser beam half-angle of intersection  $\gamma$ , and  $d_p$ , the width of the *image* of the triggering area in the LDV probe volume (given by the width of the eight trigger elements of the diode array divided by magnification of the collection optics,  $d_t=1[\text{mm}]/G \times 8 = 12.2 \times 8 \cong 98 \mu\text{m}$ ). Assume, for the

<sup>32</sup> Eight channels were used in the measurements of this chapter. In Chapters 4 and 5, ten channels were empirically selected given the size range of the particles.

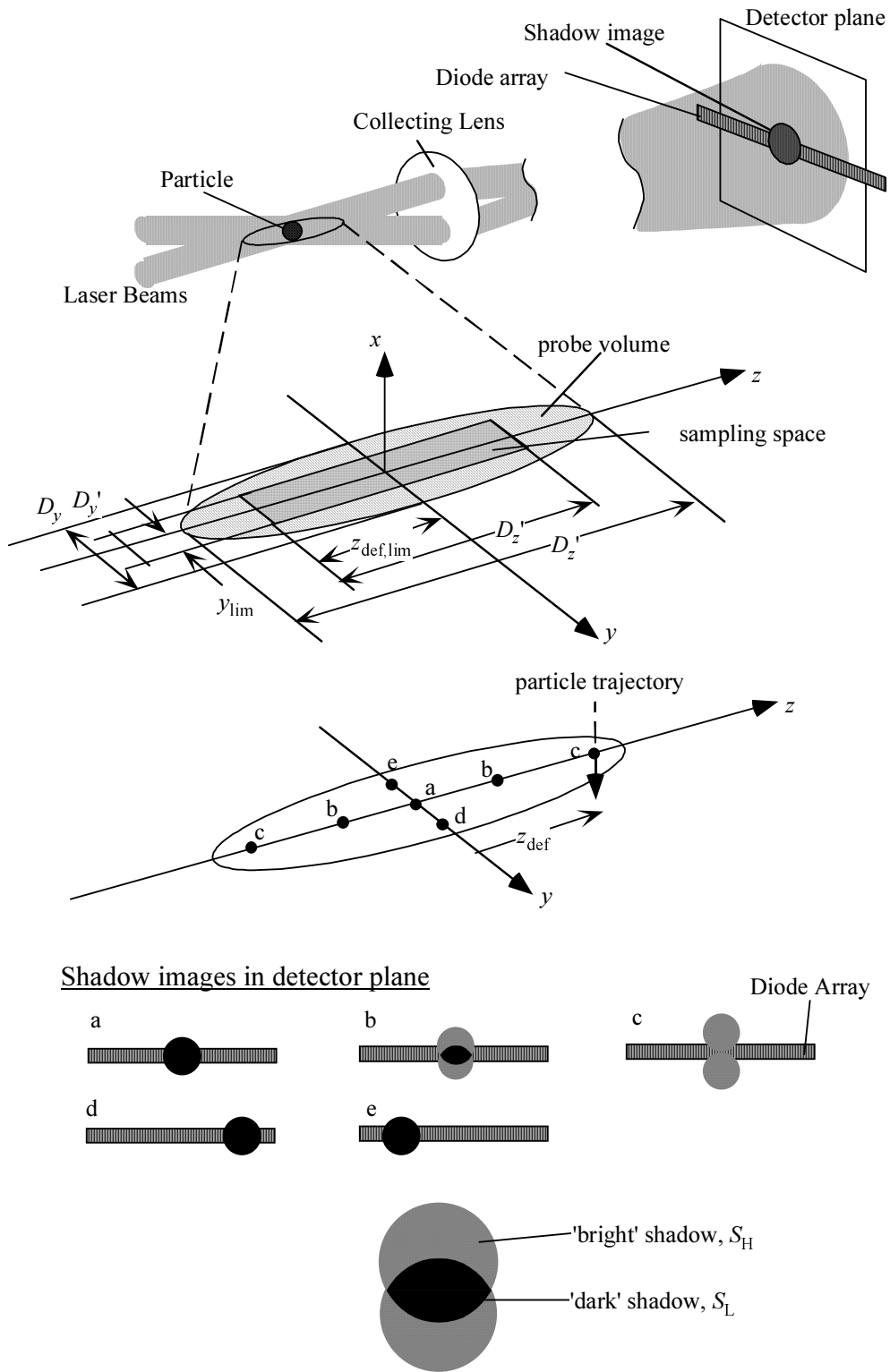


Figure 2.9 Details of the SDV sampling-space through which the particle volume flux was measured indicating the coordinate system and the dimensions defined in the text. In addition, examples of shadow images on the detector plane are also shown as a function of particle position in the LDV probe volume.

moment, that the linear array and that  $D_y$  (figure 2.9) are indefinitely large. Then the width of the cross-sectional area of the sampling-space  $d_w'$  (which depends on particle size and the number of trigger diodes, rather than on the width of the laser beam interference region) is:

$$d_w'(d_p, z_{\text{def}}) = \sqrt{d_p^2 - 4z_{\text{def}}^2 \cdot \tan^2 \gamma} + d_t \quad (2.17)$$

Figure 2.10 shows the increase of  $d_w'$  with particle size, calculated for defocus distance  $z_{\text{def}}$  of 0 and 300  $\mu\text{m}$  using equation (2.17) for the present optical parameters. Owing to the small beam intersection angle  $2\gamma$ ,  $d_w'$  is almost independent of particle size, for sizes over about 50  $\mu\text{m}$ , and of the defocus distance,  $z_{\text{def}}$ .

We now take into account that the diode array *has* finite length and thus can image only a finite portion of the optical probe volume. Let  $W$  be the width of the *image* of the detector<sup>33</sup> in the *sampling-space* of the velocimeter and which depends on the magnification of the collection optics. Morikita *et al.* (1995) showed that the width of the cross-sectional area of the sampling-space,  $d_w''$ , *decreases* linearly with particle size to avoid vignetting:

$$d_w'(d_p) = W - d_p \quad (2.18)$$

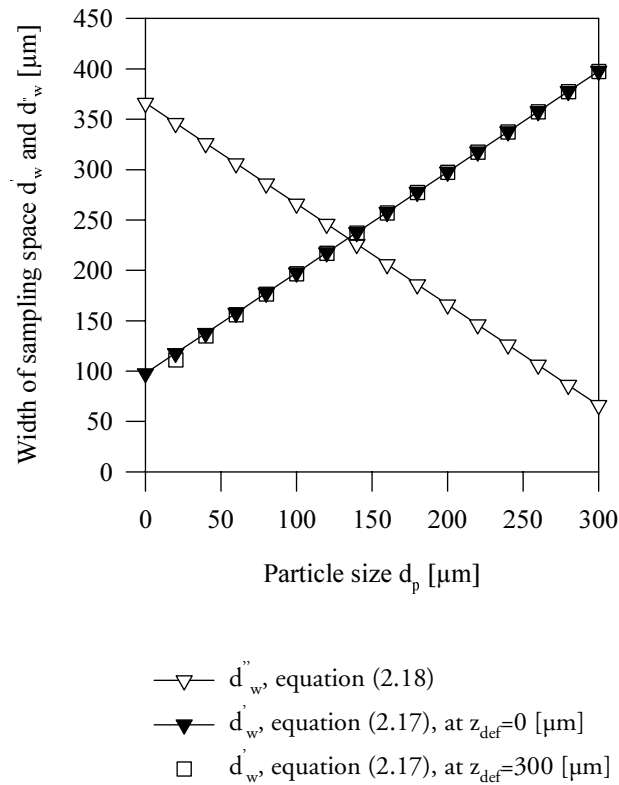


Figure 2.10 Variation of the calculated width of the sampling space as a function of particle size.

Note that  $d_t$  does not appear in this equation. The calculated values for  $d_w''$  from equation (2.18) are also plotted, as open circles, in figure 2.10. The net value of the width of the sampling-space,  $d_w$ , for any particle size is given by

$$d_w'(d_p, z_{\text{def}}) = \min(d_w'(d_p, z_{\text{def}}), d_w''(d_p)) \quad (2.19)$$

An implication of equations (2.17) and (2.18) is that the area  $A_{\perp}(d_p)$  of the sampling-space for particle size  $d_p$  with defocus limitation at  $z_{\text{def,lim}}$ ,

$$A_{\perp}(d_p) = \int_{-z_{\text{def,lim}}}^{z_{\text{def,lim}}} d_w(d_p, z_{\text{def}}) dz_{\text{def}} \quad (2.20)$$

is a non-monotonic function of particle diameter. The variation of the area of the sampling-space was estimated to be about 20% between 80 and 120  $\mu\text{m}$  particle sizes in the experiment described below, with a triggering width,  $d_t$ , of 98  $\mu\text{m}$  and a defocus limit,  $z_{\text{def,lim}}$ , of 300  $\mu\text{m}$ , for reasons given in §2.6.4.

In general, the validatable sampling-space will be *smaller* than that predicted by equation (2.20) if there are particles of random shapes and with random orientations (which was *not* the case in the experiment of §2.6.4) and particularly if the trajectories are randomly oriented relative to the axis of the photodiode array (which *is* true in any turbulent flow). The latter will be vignetted by the detector, and consequently rejected by software, which is not accounted for in equations (2.18) and (2.20) (Hardalupas *et al.* 1994). Figure 2.11 shows a pseudo-image, *i.e.* the output of the linear detector array as a function of time, which illustrates these cases: in figures 2.11 (a) and (b) a spherical particle passed through the sampling-space at trajectory angles relative to the axis of the array of  $90^\circ$ , case (a) and other than  $90^\circ$ , case (b). The trajectory in figure 2.11 (a) will be accepted but that of figure 2.11 (b) will be rejected by software because during the course of trajectory, part of the shadow image was vignetted and not recorded, although the particle, *at the time of triggering*, lies within the area defined by equation (2.20). Figures 2.11 (c) and (d) illustrate the first of two possible effects of particle shape and orientation for the particular case of identical ellipsoids with an aspect ratio of about two and trajectory normal to the diode array axis, passing through the centre of the probe volume. The choice of ellipsoids is for the sake of example only and does not limit the generality of application of the conclusions drawn here. Inspection shows that the width of the validatable cross-sectional area of the sampling-space in figure 2.11 (c) is larger than in figure 2.11 (d).

<sup>33</sup> corresponding to the 30 segments of the diode array.

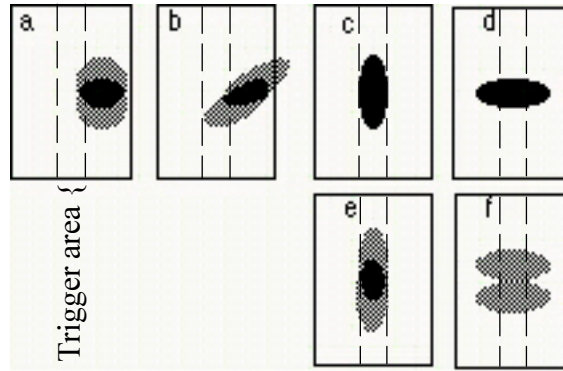


Figure 2.11 SDV image in image buffer for different cases: spherical particle at (a)  $90^\circ$  and (b) other than  $90^\circ$ ; ellipsoid in-focus (c) and (d) and defocused (e) and (f). The width of the frame surrounding each image represents the width of the active diodes of the array. The height represents samples of the array as a function of time.

Figure 2.11 (e) demonstrates the second effect, which is to limit the maximum defocus distance up to the point at which the two shadows just overlap. Particles with the orientation of figure 2.11 (e) can have larger maximum defocus distances than with the orientation of figure 2.11 (f) before they fail to trigger the instrument, and the length of the validatable area of the sampling-space will be therefore bigger. The magnitude of these two effects depend on the details of particle shape and orientation.

In order to avoid biasing of the flux and volume fraction measurements due to the effects illustrated in the preceding paragraph, an additional spatial limitation was introduced in *post-processing software* to restrict the sampling-space along the  $y$  axis, which also simplified the shape of the sampling-space to a rectangle (figure 2.9). Thus, only images, the centre of which lay within  $y < d_w$ , were accepted in the *post-processing software*, where  $d_w$  was calculated from:

$$d_w = 2y_{\text{lim}} \quad (2.21)$$

and  $y_{\text{lim}}$  is a limiting distance along the  $y$  axis, measured from the centre of the array. This dimension was set at  $100 \mu\text{m}$ , empirically, by finding the area of the sampling-space over which the measured particle arrival rate (number of measurements made over a given time) was uniform. By introducing the spatial limit,  $y_{\text{lim}}$ , the area of the sampling-space varied by only 15% over the measured size range in the experiment described below.

### 2.6.4 Experimental results

#### Accuracy of Estimation of the size of the Sampling-space

In order to apply the method described in §2.6.3 for the calculation of the sampling-space, it is first necessary to establish the error of measurement of the location of the particle in the sampling-space. The particle position in the  $y$  direction of figure 2.9 can be measured from the position of the recorded two dimensional image, by calculating the position of the ‘weighted-centre’ of the shadow image. The uncertainty was due to the discretisation error, corresponding to the half-pitch of the detector, in determining shadow displacements in the  $y$  direction: for the magnification used in this experiment, this corresponded to an uncertainty of  $\pm 6 \mu\text{m}$  in the present configuration, or  $\pm 3\%$  of the width of sampling-space, from equation (2.21), used in the present experiments.

The position in the  $z$  direction (defocus,  $z_{\text{def}}$ ) was deduced from the measurement of the separation between the two shadow images described earlier. However, the uncertainty of the measurement of the defocus was expected to be worse than that in the  $y$  direction due to the resolution  $\Delta z$ , as a result of the small intersection angle.<sup>34</sup> In order to quantify the uncertainties, an experiment was carried out using a  $100 \mu\text{m}$  pinhole by Morikita (1996) and his results are presented here. The size of the pinhole was arbitrarily chosen because the error on the defocus measurement is dependent only on the separation between the two shadow images. The pinhole image, which extended over approximately 8 segments of the diode array, was fixed on an optical flat on a rotating disk driven by a servomotor mounted on a three-dimensional traverse to provide a stable and reliable signal source. The pinhole was rotated with a velocity about  $1.5 \text{ m/s}$  and the rotational drifting was smaller than  $2\%$ . This technique was proposed by Hovenac and Hirleman (1991).

Figures 2.12 a and b compare the mean and rms of the SDV-measured defocus with the true defocus for four trajectory angles, which were varied by traversing the rotating disk. The measured mean pinhole defocus distance, over 100 measurements, collapsed on a single curve for defocus distances between  $100$  and  $500 \mu\text{m}$ , with systematic error smaller than  $8\%$  except in the region with defocus smaller than  $100 \mu\text{m}$ . This systematic error was probably due to error in measurement of the intersection angle which, for practical reasons, had to be measured from triangulation limited to the transmitting optics side. The large departures from the actual defocus distance in the region of  $0$  to  $100 \mu\text{m}$  were due to the response time of the detector array, which was not fast enough to detect the sharp signal changes from the shadow passage. The random error was always smaller than  $50 \mu\text{m}$  and typically  $20 \mu\text{m}$ , which corresponded to  $7\%$  if the sampling-space dimension in  $z$  direction was larger than  $600 \mu\text{m}$ . In any case, a random error does not affect the measurement of  $G_{\perp}$  (less than  $1\%$  if the sample size was more than  $100$ ) and only the systematic error of  $8\%$  was considered in the further discussion. As a consequence, the systematic error in the determination of  $A_{\perp}$  was  $8\%$ .

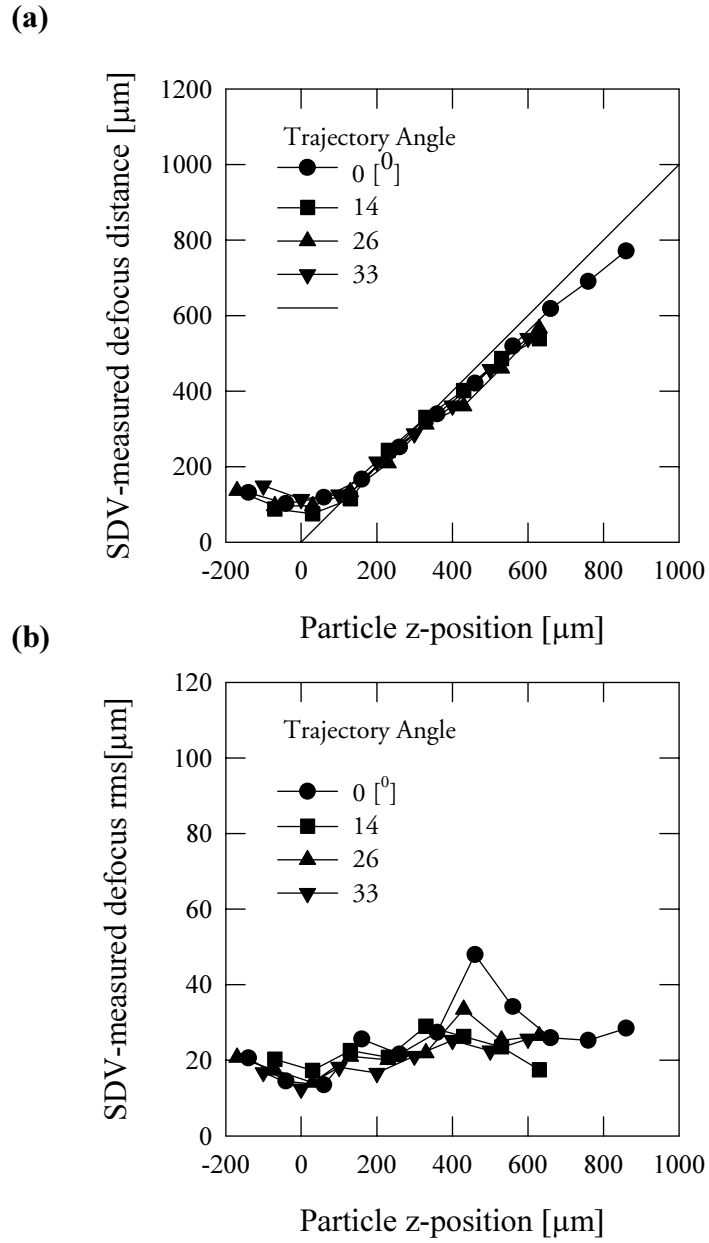


Figure 2.12 (a) mean and (b) rms SDV-measured defocus distance of a pinhole shadow image for four trajectory angles relative to the axis of the array.

<sup>34</sup> Large intersection angles are generally prohibited by the diameter of the receiving lenses and the requirement to collect the laser beams which contain the shadow information, as described in the optical arrangement (§2.2).

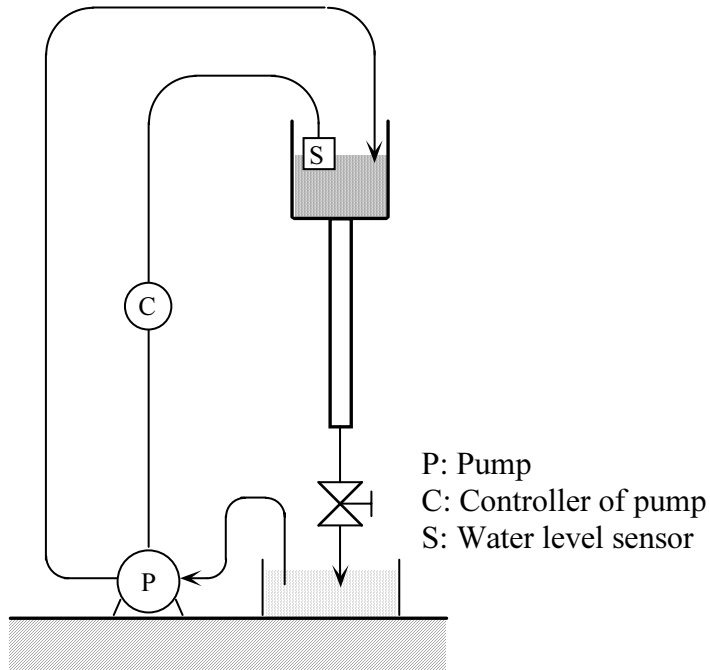


Figure 2.13 Schematic of the water-flow channel.

### Flux and Volume Fraction Measurement

The accuracy of flux measurement was estimated by comparison with measurements in a flow with known particulate mass flux and volume fraction. In the present study, a water channel flow laden with polyethylene spheres was used, as shown in figure 2.13. A closed water circuit was arranged by using a vertical rectangular duct 550 mm long with  $20 \times 20 \text{ mm}^2$  square cross-section connected to an electronically controlled pump. The bulk water velocity was 0.16 m/s and the corresponding Reynolds number  $3.2 \times 10^3$ . Pre-weighed batches of monodisperse polyethylene particles (SB-100S, Asahi Kasei, Japan) of 100  $\mu\text{m}$  nominal, company-quoted diameter were mixed in a known water volume and thoroughly stirred to form a uniform mixture. The uncertainty of the precision balance was smaller than 0.1% of the total particulate mass suspended in the water. The drift velocity between the continuous and the dispersed phase was expected to be negligible, because the density of the particles was  $1055 \text{ kg/m}^3$ , very close to that of water and it is therefore a reasonable approximation to assume that the velocity of the continuous phase was that of the particles.

Particle mass flow rate was evaluated by integration of the local flux at 20 points over the cross sectional area at 450 mm below the inlet of the duct, as illustrated in figure 2.14, for the case of bulk volume fraction, or loading, of 0.005%. The error due to numerical integration, which was estimated from comparison between best and worst results using numerical

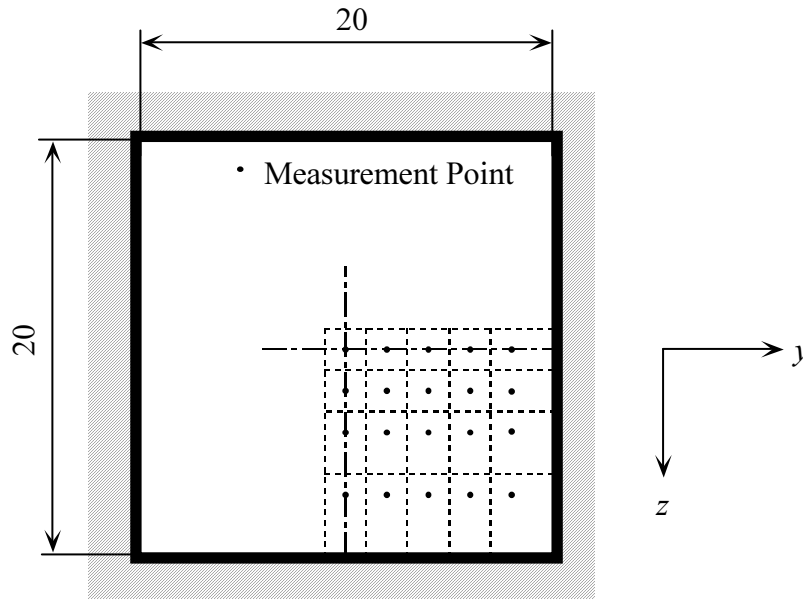


Figure 2.14 Location of measurement points in a cross section of the flow channel of figure 2.13 used for the integration of the local flux.

integration schemes of first and second order of accuracy, was estimated to be smaller than 12% and was considered to be random. In addition, from the integration procedure it was estimated that the measured particle loading on the centreline was larger than the bulk value by a factor of 1.3 as might be expected from the ratio of centreline to bulk velocity in a turbulent pipe flow. The bulk volume fraction was then derived by dividing the mass flow rate by the bulk velocity, based on the bulk particle velocity established by integration and the assumption that the particle and continuous phase velocity were identical, and the known cross-sectional area of the duct. The bulk particle volume fraction was *estimated* from a single flux measurement in the centre of the duct at all other loadings, by correction with the empirical factor estimated for the case of 0.005% volume loading. This was a reasonable approximation, since the volume fraction profiles were expected to be similar for the range of volume loadings considered here because particle-particle interaction is negligible. For the determination of the local flux, equation (2.13) was applied. The size of the area of the sampling-space was calculated from equation (2.21) but, following the analysis of §2.6.3,  $y_{lim}$  in equation (2.21) was chosen to be 100  $\mu\text{m}$  and that resulted in a rectangular cross-sectional area for the sampling-space which satisfied the requirements for minimum width of the sampling-space from equations (2.17), (2.18) and (2.21).

In principle, the measured mass flux should be independent of the size of the sampling-space, because the particle density is presumably uniform within the probe volume. However, because of the finite response time of the detector and the so-called cockscomb appearance of the

leakage error associated with the use of the “adjusted Gaussian fitting” functions for interpolation of the correlation-based measurement of defocus distance (Kobashi *et al.*, 1990; Ibrahim *et al.*, 1990), the measured flux varied with defocus limitation. Thus, for a uniform distribution of particles in the  $z$  direction, the probability density function of *measured* defocus distance would

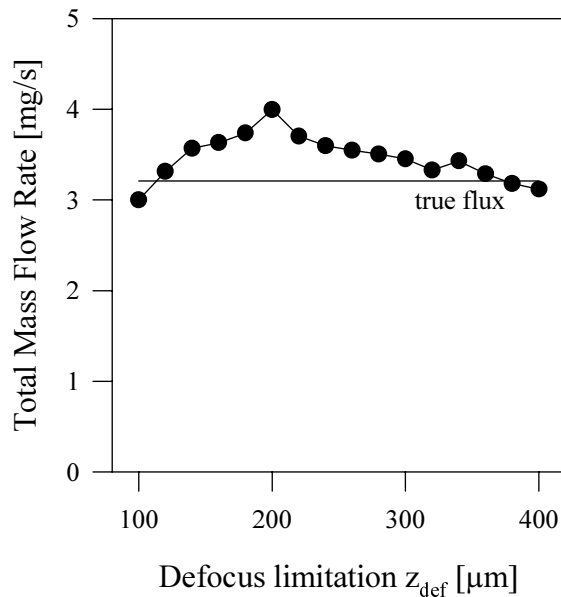


Figure 2.15 Variation of the particulate mass flow rate (●) as a function of the defocus limitation  $z_{\text{def,lim}}$  in comparison with the true flow rate (solid line).

not be uniform but could have a quasi-sinusoidal cockscomb variation about the mean, with wavelength related to  $\Delta z$ . To minimise the error associated with this variation, it is necessary to make the value of  $z_{\text{def,lim}}$  as large as possible. Figure 2.15 presents the measured particulate mass flow rate (circles), over 1000 measurements for each point, as a function of defocus limitation, compared to the mass flow rate (solid line, calculated from the particle mass and water volume) of 3.21 mg/s for the case of 0.005% volume fraction and  $0.119 \text{ mm}^{-3}$  calculated number concentration. The raw data, stored in the computer, for this figure was *the same for each point* and the defocus limitation was applied in post-processing software: the calculated particulate flux was within -7% and +25% of the SDV-measured value and the variation is due to the cockscomb leakage effect. It is observed that the flow rate increases linearly with defocus for distances smaller than 200  $\mu\text{m}$ , due to leakage effects and the use of  $\Delta z \approx 100 \mu\text{m}$ , and then decreases towards the true value. For defocus distances larger than 500  $\mu\text{m}$ , the sizing error becomes larger than the 10% random error in the estimation of the area of the sampling-space, which again results in high uncertainties in the calculation of the flux. As a rule of thumb, the minimum defocus distance,  $z_{\text{def,lim}}$ , should not be smaller than that corresponding to separation between the two shadows equivalent to 2 diode segments (about

250  $\mu\text{m}$  in the present configuration) and not larger than 500  $\mu\text{m}$ , because the sizing error becomes comparable to the error in calculating the sampling-space. A value of  $z_{\text{def,lim}}$  of 300  $\mu\text{m}$  was therefore adopted in this work.

The uncertainties of the quantities related to the mass flux measurement are summarised in Table 2.2. The *systematic* uncertainty of the integrated particle volume was estimated from comparison of the SDV-measured mean diameter and the maker-specified diameter. The *random* uncertainties in the measurement of a particle diameter, the position along the detector and the defocus distance which were (0.5/8) or 6%, 3% and 7% respectively, do *not* contribute to the total uncertainty in the flux measurement, because volume flux was estimated from average quantities over a large sample and according to the central limit theorem, the variance of the mean (*i.e.* the standard error of the mean) decreases with increasing sample size.

**Table 2.2: Estimated systematic uncertainties of the mass flux measurement at a point.**

Particle volume $V(i)$	6%
Area of sampling-space $A_{\perp}(i)$	8%
Mass flux $G_{\perp}(i)$	
Particle volume fraction $C_v$	$\cong 14\%$

Figure 2.16 shows comparison between the SDV-measured (blocked circles) against the actual (solid line) particulate integrated volume fraction on log-log axes. The vertical uncertainty bands denote the expected systematic uncertainty according to Table 2.2. We chose to base the comparison on integrated particle volume fraction, rather than on mass flow rate, because the reference values were a known mass of particles, of known material density, and a known volume of water in the flow circuit, so that the bulk volume fraction is more accurately known than is the mass flow rate of particles in the duct.

For dilute flows with volume fraction up to 0.005%, the discrepancy did not exceed 20% and the observed discrepancy in figure 2.16 is, taking into account the systematic errors listed in Table 2.2 together with 12% of the systematic error due to flux profile integration, no worse than is to be expected. However, the measured flux was consistently smaller than the actual value for volume fractions larger than 0.005%. This difference was caused by the turbidity of the flow (*e.g.* Kliafas *et al.* 1987) and most of the rejected signals were interpreted by the software as multiple occupancy of the sampling-space; it was even observable by eye that the incident laser beams were partly extinguished by their passage through the flow. The dense-flow limitation of the instrument on the basis of the present measurements was estimated in the order of 0.005% in volume fraction: to provide a comparison, this would be equivalent to a mass loading of 5% for water droplets in an air flow in the duct.

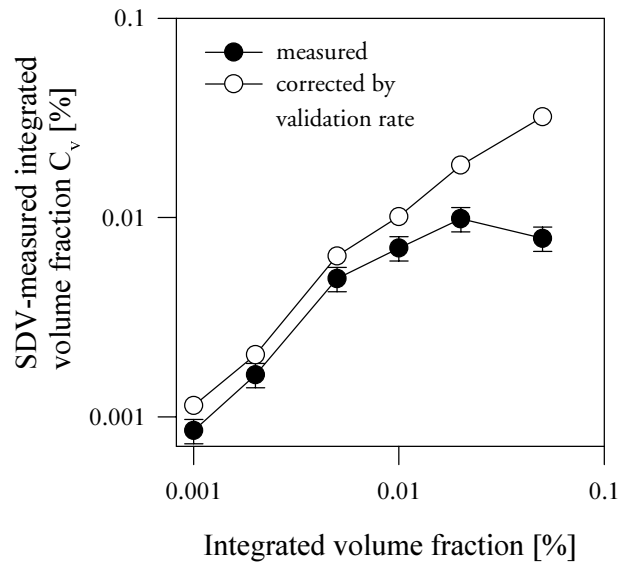


Figure 2.16 Comparison between the measured (●) against the actual (solid line) integrated particulate volume fraction. Open circles correspond to the fraction corrected by the signal error rate of the SDV

The larger discrepancy in figure 2.16 for integrated volume fraction higher than 0.005% is likely to be a result of beam extinction due to multiple particle occupancy along the beam path. As a consequence, the discrepancy should correlate with the number of rejected measurements. Indeed, figure 2.17 shows that the signal error rate (rejected signals / validated

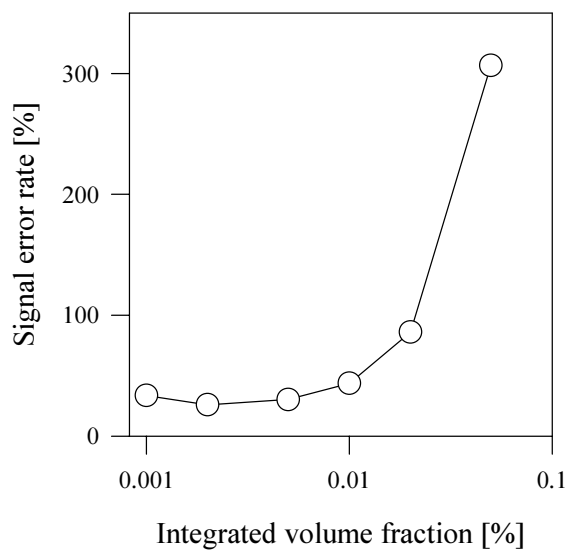


Figure 2.17 Signal error rate as a function of volume fraction.

signals, where signals were rejected *either* because the particle location was outside the user-set defocus limitation,  $z_{\text{def,lim}}$ , *or* because the cross-correlation routine suggested multiple-occupancy of the probe volume). In figure 2.17, it should be noted that, for volume fractions below about 0.01%, the signal error rate of about 20-30% was overwhelmingly due to particles being beyond  $z_{\text{def,lim}}$  and hence the signal error rate does not, in principle, contribute to an error in mass flux measurement. In contrast, the signal error rate increased rapidly with volume fraction above a volume fraction of 0.01% and this was overwhelmingly due to multiple occupancy. This result suggested that correction of the flux measurement by the signal error rate can provide a reasonable estimate of the flux particularly for fractions above 0.01% v/v; the open circles in figure 2.16 correspond to the corrected values of the measured fraction. As expected, better agreement for the dense limit of the present measurements was achieved from the correction procedure and the maximum discrepancy did not exceed 40% for the worst case, compared with the almost 100% for the uncorrected values.

### 2.6.5 Extension to residence-time based volume fraction measurement

The features of the method described in earlier sections imply that it is possible to calculate residence time-based volume fraction using equation (2.16). In that case, the particle residence time  $\tau(i,j)$  through the sampling-space must be determined from the analogue signal, *i.e.* the signal before passing through the window comparators, which in turn implies that this time will be a function of the threshold levels used for the discrimination of the shadows, figure 2.18. The uncertainty in the determination of the residence time arises from the shape of the

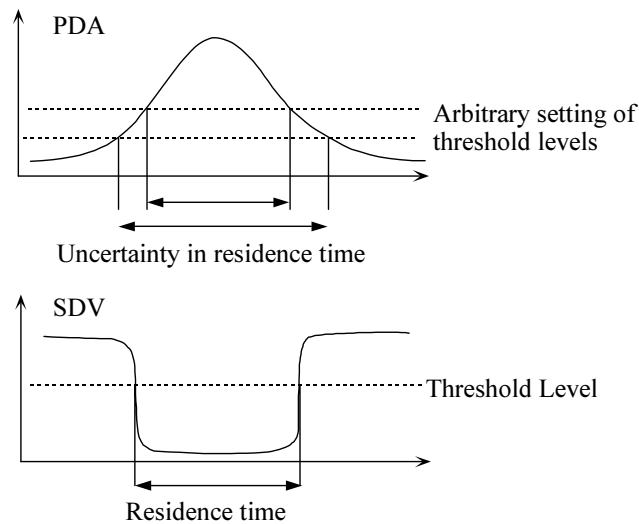


Figure 2.18 Schematic of residence time calculation as a function of threshold levels, for PDA and SDV respectively.

analogue signal which rises and falls more sharply than the raw signals from LDV. Thus, according to the results of Hardalupas *et al.* (1994), the error in the estimation of a transit time will be exactly that involved in the determination of diameter and hence will not exceed 10% for irregular, powder-like particles. However, the method of §2.6.3 must now be extended to calculate the volume  $V_s(i)$  of the sampling-space as a function of the trajectory and the particle shape and size.

The volume of the effective sampling-space of the SDV can be determined from the area of the sampling-space, following the analysis of §2.6.3, together with the relevant dimension in the  $x$  direction of figure 2.9. This dimension will be the size of a sampled particle, because the instrument is triggered as long as there is particle passing through the sampling-space. The volume thus is given by

$$V_s(i) = D'_y \cdot D'_z \cdot d_p(i) \quad (2.22)$$

where  $D'_y = 2y_{\text{lim}}$  and  $D'_z = 2z_{\text{def,lim}}$  are the sizes of the sampling-space in the  $y$  and  $z$  direction, respectively, as shown in figure 2.9 and  $d_p(i)$  is the nominal diameter of particle size class  $i$ . As for single-component LDV and PDA systems, this analysis holds if the  $x$  velocity component is larger than the  $y$  and  $z$  components, or, in other words, if the flow is almost normal to the axis of the photodiode array. Again as in LDV and PDA systems, if the latter condition is not satisfied, large uncertainties in the measurement of particle volume fraction are likely to arise.

When the particle is non-spherical, asphericity of the particle could cause measurement error on flux, similar to the effect illustrated in figures 2.11(c) and (d). To avoid this effect, use of the area-equivalent diameter,  $d_p$ , in equation (2.12) will suffice, assuming that the particle passes the probe volume with random orientations. Although the volume fraction defined by equation (2.16) is equivalent to the result from equation (2.14) *in the present condition*, since the particle used in the experiment is spherical and the flow was uni-directional, the technique can be used to obtain residence-time based volume fraction measurement, as well as the velocity-based value.

## 2.7 Trajectory Bias Effects

Since the sizing technique is based on a linear photodiode array, size-validated measurements can be obtained only when particle velocity exceeds about 0.5 m/s, a limit which has been experimentally determined (see figure 2.19). This limit is due to the fact that the shadow

---

<sup>35</sup> Which was aligned to coincide with the “streamwise”, or axial flow velocity except for the measurements in the downstream region of the confinement of Chapter 3, where the array was not aligned with any cartesian velocity components.

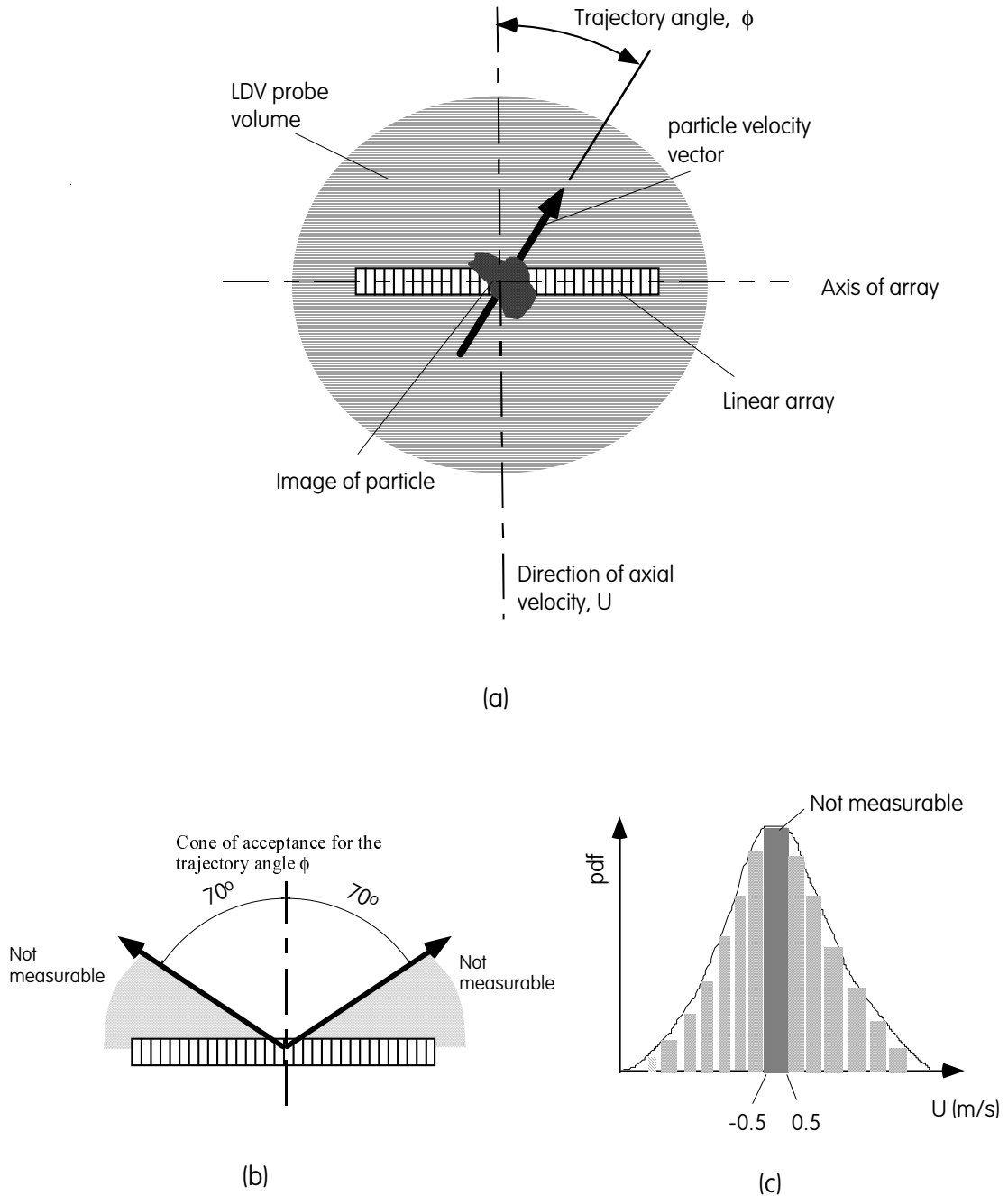


Figure 2.19 Velocity bias effects due to SDV; (a) shows a schematic of the image of the LDV probe volume on the diode array and a particle trajectory through the probe volume at angle  $\phi$  relative to the normal to the array, (b) the range of experimentally-determined measurable trajectory angles  $\phi$  and (c) the range of non-measurable velocities normal to the array which are missing from the velocity pdf.

image of a particle *must* travel over the array, so that a finite number of one-dimensional slices is obtained before the particle projected image can be reconstructed. If the shadow image of a particle were travelling with velocity which was practically zero, as could have happened in the region of a recirculation zone, then the one-dimensional slices obtained during sampling would

correspond to the same position of the particle and no particle image could be reconstructed. In addition, particles which have mean velocity normal to the array<sup>35</sup> are likely to have finite mean velocity along the detector or follow the high fluctuations in the region of a stagnation point and, therefore, are likely to travel parallel to the detector end cover, at some point, the extreme diodes of the array. The latter is a cause for rejection as shown in §2.8.

For a similar reason, a measurement will be validated, provided that the trajectory of a particle is not parallel, or near-parallel, to the axis of the photodiode array, which in practice means that only particles with trajectories at angles  $\phi$  smaller than about  $70^\circ$  will be measured, figure 2.19b. A consequence of these two effects is that there is a combination of particle trajectories and velocities which will not contribute to the particle velocity statistics and it is therefore necessary to investigate theoretically the extent of velocity biasing caused by these two effects. A parametric investigation, based on a Monte Carlo simulation was selected for this analysis, because it allowed realistic representation of a turbulent fluid flow field and the angle- and velocity restrictions mentioned earlier. The underlining idea behind the simulation is the following: a flow field is assumed with mean axial and radial velocities  $\bar{U}$  and  $\bar{V}$  whilst turbulent fluctuations in these directions are characterised by rms values  $\sqrt{\overline{u^2}}$  and  $\sqrt{\overline{v^2}}$  respectively, which are Gaussian-distributed around the mean velocities and also have a mean  $\sqrt{\overline{uv}}$  correlation. The simulation is performed by sampling randomly the Gaussian distributions for the axial and the radial velocity fluctuations and estimating the turbulent velocities from:

$$\begin{aligned} u &= (\overline{u^2})^{\frac{1}{2}} P_1 \\ v &= \frac{\overline{uv}}{(\overline{u^2})^{\frac{1}{2}}} P_1 + \frac{(\overline{u^2 v^2} - \overline{uv}^2)^{\frac{1}{2}}}{(\overline{u^2})^{\frac{1}{2}}} P_2 \end{aligned} \quad (2.23)$$

the derivation of which is explained in Appendix I. In this equation,  $P_1$  and  $P_2$  are random variables, sampled from a Gaussian probability density function. Following sampling, the instantaneous velocities are:

$$\begin{aligned} U &= \bar{U} + u \\ V &= \bar{V} + v \end{aligned} \quad (2.24)$$

and the constraints for the axial velocity and the trajectory angle mentioned above are imposed on  $U, V$  pairs for which both following conditions hold:

$$|U| > 0.5 \quad (2.25a)$$

$$\left| \tan\left(\frac{V}{U}\right) \right| < \left| \tan(70^\circ) \right| \quad \text{"cone of acceptance"} \quad (2.25b)$$

were included in the calculation of the SDV-measurable velocity statistics. A total of 100000 samples were used which resulted in statistical uncertainty of less than 0.5% in the rms velocities. It should be noted here that for simulated conditions presented below, which correspond to those of the experiments, typically 10-20% of the samples were rejected because they did not satisfy the velocity and trajectory angle constraints, but the statistical uncertainty did not exceed 1% in most simulations.

Figure 2.20 shows indicative results from the simulation to demonstrate the effect of increasing the “true” rms of the fluctuations of the axial velocity on the measured mean axial and radial velocity, the radial rms and the cross correlation, with the “true” mean axial velocity as parameter. The results presented in the figure are for mean radial velocity of 1 m/s, radial rms of 2 m/s and cross correlation coefficient of 0.3 which are typical values measured in the flows of Chapter 4. The calculated range of axial rms velocities was from 1 to 8 m/s, but values in the range of 2 to 5 m/s are likely to be measured. The calculation extended to values higher than those of practical interest in order to demonstrate the asymptotic behaviour of the quantities sampled by the Monte-Carlo method with increasing axial rms velocity. The selection of the axial mean velocities over which the calculation was performed was arbitrary, but nevertheless sufficient for the investigation, as it spans the range of mean axial velocities which were measured in the neighbourhood of the recirculation zone of Chapter 4, as well as axial velocities which are encountered away from it. Although results are presented for positive mean axial velocities, extension to negative ones is straightforward and results have shown that in those cases the deviations have the same sign as the ones presented, *i.e.* quantities which are *overestimated* when the mean axial velocity is positive are *overestimated* by the same amount when the mean axial velocity changes sign. The estimated (*i.e.* simulation of the measured) quantities are plotted in figure 2.20, normalised by the initial values of the Gaussian distributions.

A feature of all plots in figure 2.20 is that only under conditions which correspond to a mean axial velocity of 10 m/s, are the computed and the actual values for the mean and the turbulent quantities within about 3% of each other, and deviations from the actual values increase with decreasing mean axial velocity and its rms. This is expected due to the two potential sources of bias in equation (2.25), and especially the effect of the cone of acceptance for the trajectory angles. In principle, this effect will be important when the instantaneous radial velocity is around 2.5 times larger than the instantaneous axial velocity. The probability of occurrence of such unfavourable instantaneous velocity ratios and thus, rejected instantaneous trajectory angles, decreases with increasing *mean* axial velocity and axial rms velocity. Moreover, the computed mean axial velocity as well as the cross-correlation coefficient are systematically

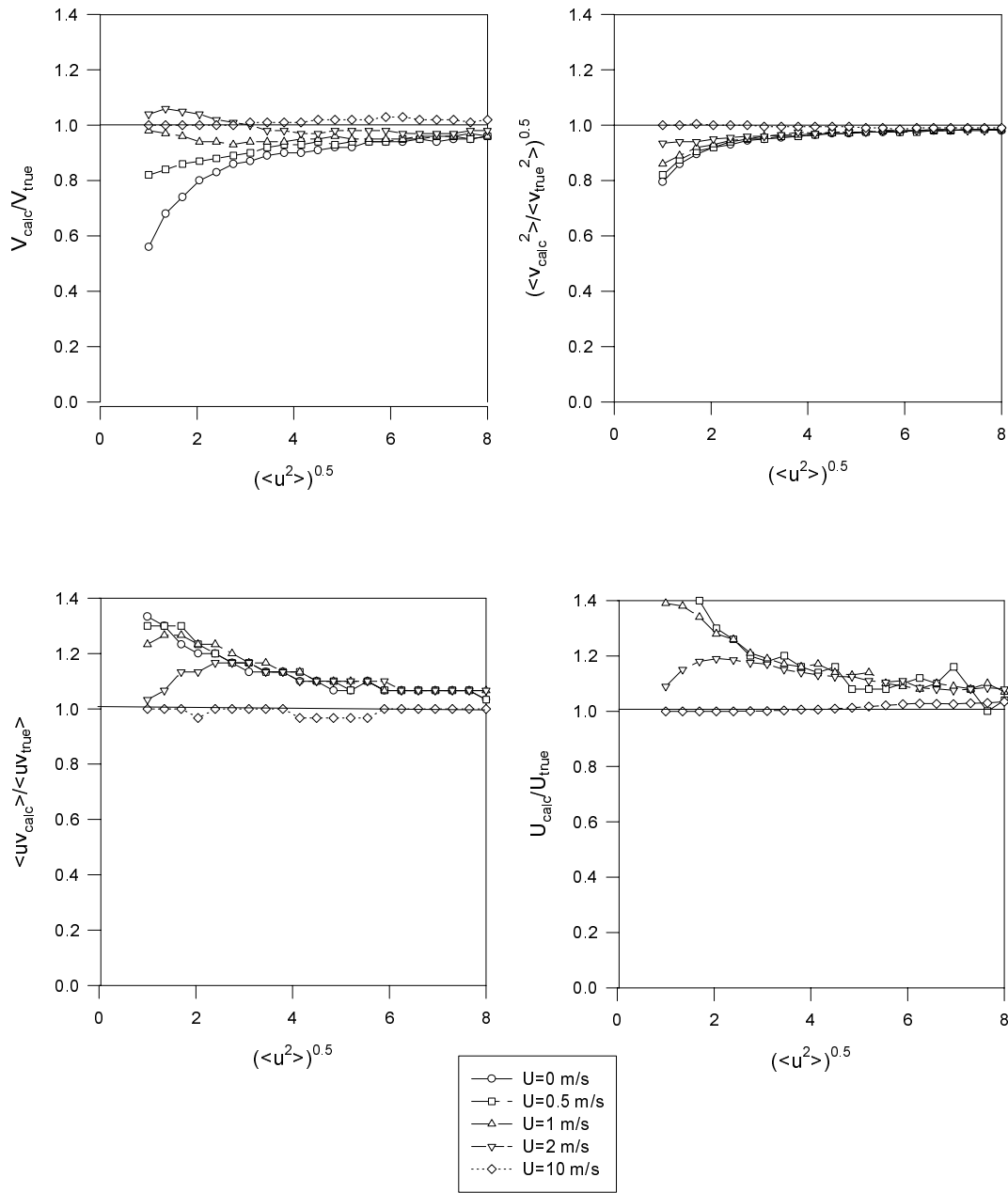
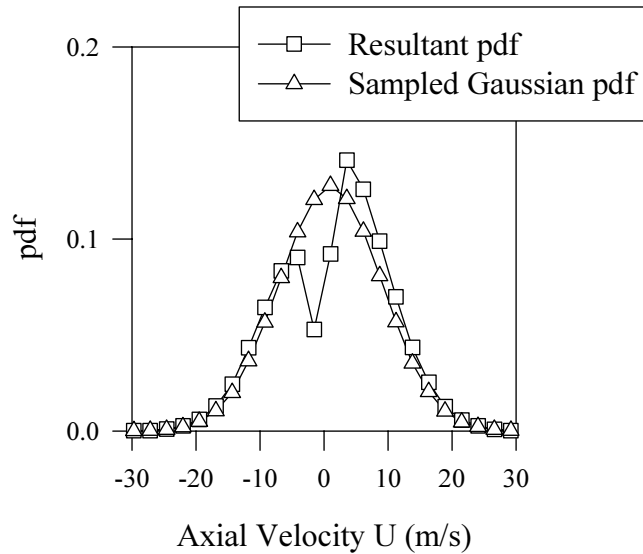


Figure 2.20 Variation of the normalised calculated mean axial and mean radial velocity, the normalised rms radial and the normalised velocity cross-correlation as a function of the axial rms velocity for a range of mean axial velocities, using Monte-Carlo simulation. Symbols as in legend.

overestimated and the mean and rms radial velocities are systematically underestimated. Inspection of the curves for zero mean axial velocity suggests that the deviations from the actual values must be owing to the effect of the trajectory angle, equation (2.25b), since the gap in the velocity pdf due to unmeasurable small axial velocities due to equation (2.25a)--those



*Figure 2.21 Calculated axial velocity pdf as compared to the sampled Gaussian, for conditions: mean axial velocity  $U=1$  m/s, mean radial  $V=1$  m/s, rms axial velocity  $u=8$  m/s and rms radial  $v=2$  m/s.*

between  $-0.5$  and  $0.5$  m/s— is symmetrically distributed in the pdf when the mean is zero (figure 2.19c). Thus, since the mean axial velocity is affected, as can be observed in figure 2.20 the effect must be due to equation (2.25b).

Figure 2.21 presents example of sampled Gaussian and its resultant pdf, created after imposing the velocity and trajectory angle limitations from equation (2.25a), for a flow with 1 m/s mean axial and radial velocity and 8 m/s and 2 m/s for the respective rms, which are typical measured values in the region of the recirculation zone. The characteristic of the resultant pdf is that a part of the distribution is missing, due to the velocity and angle limitations, but it does not drop to zero, as one would expect for the velocity range from  $-0.5$  to  $0.5$  m/s, due to the 2.5 m/s wide velocity bins used to construct the distribution. The maximum in the resultant pdf shifted from 1 m/s towards larger velocities, because the limitation for the trajectory angle resulted in rejection of axial velocities smaller than 1 m/s, where the ratio  $V/U$  and, therefore, the angle became large.

In fact, the measured axial velocity pdf in the region of the free stagnation point associated with the mean recirculation zone was never Gaussian in the experiments of Chapter 4 but bimodal. The effect of the aforementioned limitations on the measured axial velocity pdf is likely to be different to those presented in the previous paragraph, which were produced by simulating the velocity distribution as Gaussian. For this reason, statistical analysis of the measured raw data was carried out in order to demonstrate that the actual effect of the velocity

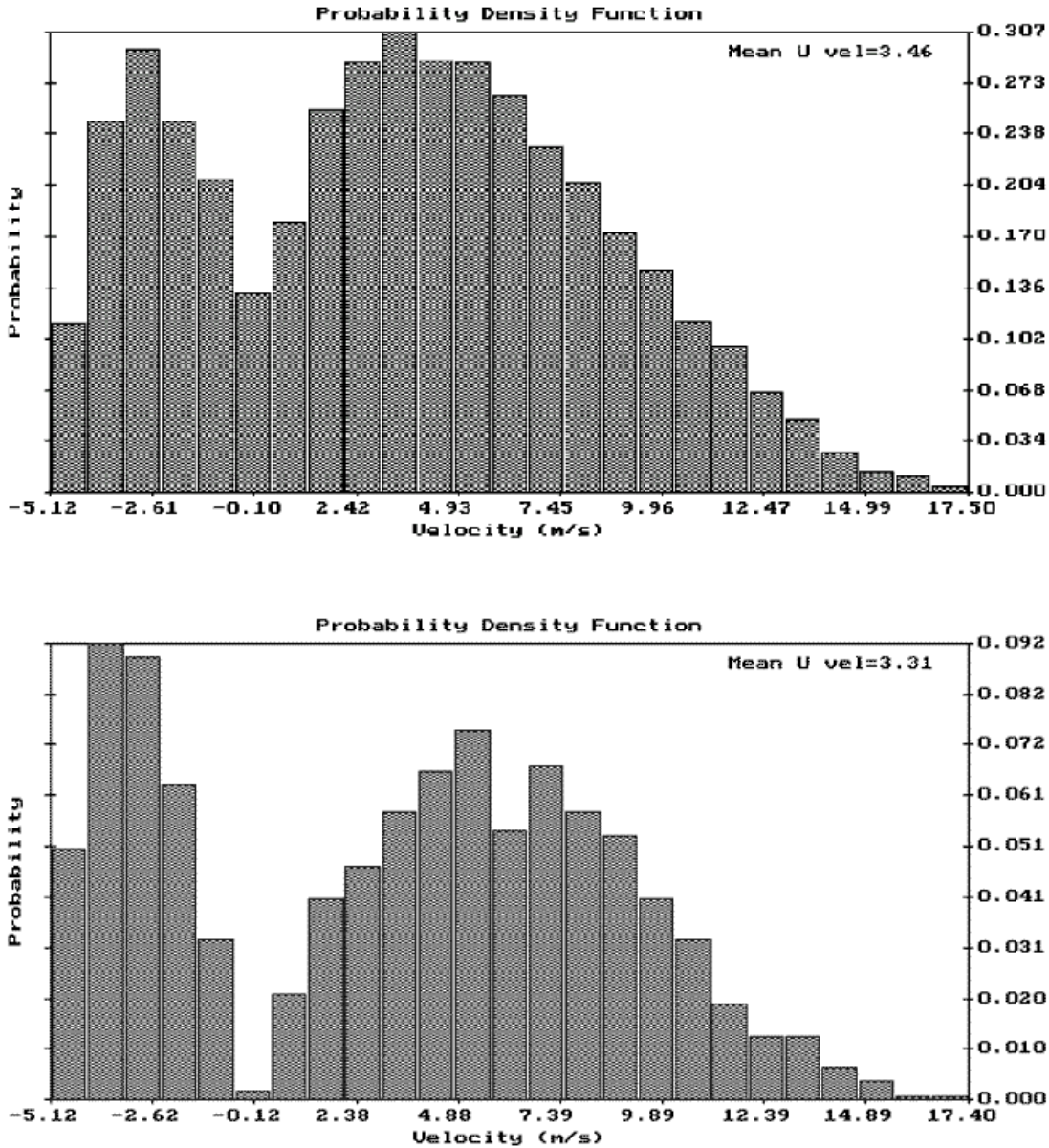


Figure 2.22 Comparison between axial velocity pdfs measured in the burner of Chapter 4, for swirl number  $S=0.41$  at  $z/D=2.67$  and  $r/D=0$ , processed to include data which were velocity- but not size-validated (top) and size- and velocity-validated data (bottom).

and angle limitations on the measured *particle* velocity pdf. This, as shown in figure 2.22, was smaller than predicted by calculations, probably due to deviation of the measured *particle* axial velocity pdf from the assumed Gaussian in the simulation. Figure 2.22 presents comparison between (a) the axial velocity pdf constructed from all measurements, either size- and velocity- or only velocity-validated and (b) the pdf constructed from only size- and velocity-correlated measurements, measured in the burner of Chapter 4, for swirl number  $S=0.41$ , at  $r/D=0$  and  $z/D=0$  (see Chapter 4 for definition of the coordinate system). This condition was arbitrarily selected from the experimental investigations of Chapter 4 and all size classes were included in

the processing. A gap in the region of zero instantaneous velocities is observed in (b), the result of the velocity-limitation, but the difference between mean axial velocities corresponding to each pdf is about of 5% providing confidence that the calculated values presented in figure 2.20 constitute worst-cases, and smaller effects of the aforementioned trajectory bias effects are expected in practice.

## 2.8 Sources of Data Rejection

A statistical analysis of two arbitrarily-selected raw data sets was performed in order to estimate the contribution of the sources of rejection of measurements to the total rejection rate –the reciprocal of the validation data rate– identify mechanisms which contribute to a particular rejection source and suggest potential remedies to decrease rejection and thus increase data rates. The latter is of great importance to complex flows like those investigated here, because high rejection rates increase the duration of experiments and this is detrimental to the materials used in confined reacting flows.

The analysis was performed by counting the rejected measurements in the raw data sets as a function of the error code produced by the software validation procedure described in §2.5.4. The results from processing are presented in bar charts below, and Table 2.3 provides the nomenclature for the reported error codes. It is recalled that the error codes presented in Table 2.3 are due to application of software validation procedures and the reader should refer to §2.5.4 for details on the validation criteria that the data failed to meet.

Figure 2.23 presents statistical distribution of sources of data rejection from measurement of a complete radial profile measured in the swirl burner described in Chapter 4 for swirl number 0.41, at (a)  $z/D=2.67$  and (b)  $z/D=4$ . It shows that the largest contribution in data rejection was from images which were clipped along the detector, and amounted to up to 20-30% of the total SDV-rejected data. The total number of rejected data decreased across the profile and had minima of 5% and 10% in the cases presented in figure 2.23(a) and (b) respectively. In view of the contribution of the almost constant contribution across a profile of about 5% due to multiple scattering, it is assumed that a large number of rejected measurements due to multiple scattering was actually rejected due to image clipping because of the validation sequence.

From the other sources, rejections due to lack of peak in the cross-correlation contributed about 5%, probably a result of optical noise, rejections due to overflow of image buffer could contribute up to 10%, as in figure 2.23(b), whilst rejections due to image clipping along the detector, failure to separate the raw image and incorrect sampling rate had insignificant

Table 2.3: Error codes presented in figure 2.23 and their description

Error code name	Error Description
IB OVERFL	Overflow of fixed-size Image Buffer where all one-dimensional slices are stored. Caused by a slow-moving large particle.
IM CL TOP/BOTT	Top/Bottom of Image was Clipped. In both cases this can be caused when the number of samples taken was too small and the image was not sampled properly, due to incorrect velocity measurement.
IM CL Ch 1/32	Image was Clipped along detector near channel 1 or near channel 32 (corresponding to the extreme segments of the diode array). Both errors are caused when a large particle passes off-centre from the array, or beam wandering through flames causes irradiance on channel 1 or 32 to fall below reference levels, and this is misinterpreted as shadow. <sup>36</sup> It can also be caused if the particle velocity component along detector axis is large compared with the component normal to it.
IM DIV FAIL	Failed to separate the defocused shadow image into two shadows because no "dark" shadow was captured near the trigger event, caused by either noise or presence of particles smaller than the equivalent of two diode pitches.
NO PEAK CC (1)	No peak in the cross-correlation function was found, <i>i.e.</i> the two images after separation were unrelated. Could only be caused by noisy signals.
NO PEAK CC (2)	The cross-correlation coefficient was 0, <i>i.e.</i> after separation only one shadow was found; caused by noisy signals.
WRONG SR	Not enough samples due to Wrong Sampling Rate. The source of this error is fundamentally different to "IM CL TOP" or "IM CL BOTT" errors and is caused when the normalised distance, $r$ , travelled by a shadow between successive samples in the direction normal to the detector is less than 0.1 - an arbitrarily selected limit. In general, the sampling rate is selected so that $r$ is around 1 or greater and, thus, occurrence of this error should be rare.
MULTSCA	Multiple scattering was found. <sup>37</sup> This error is caused when, applying correlation techniques to match the two images after separation, the non-overlapping area 50% is larger than that of the overlapping, implying presence of a parasite image.
PROBLEMATIC	Problematic Measurement, rejected either because of noise, which resulted in a single diode appearing as covered by shadow, or because an area larger than the 1/3 of the Image Buffer was covered by shadow. The latter is usually caused in reacting flows by large beam wandering which can be misinterpreted as a large shadow by the signal processor. Can be also caused by measurement of a particle with shadow image larger than the width of the array, which was accidentally validated due to its alignment with the flow

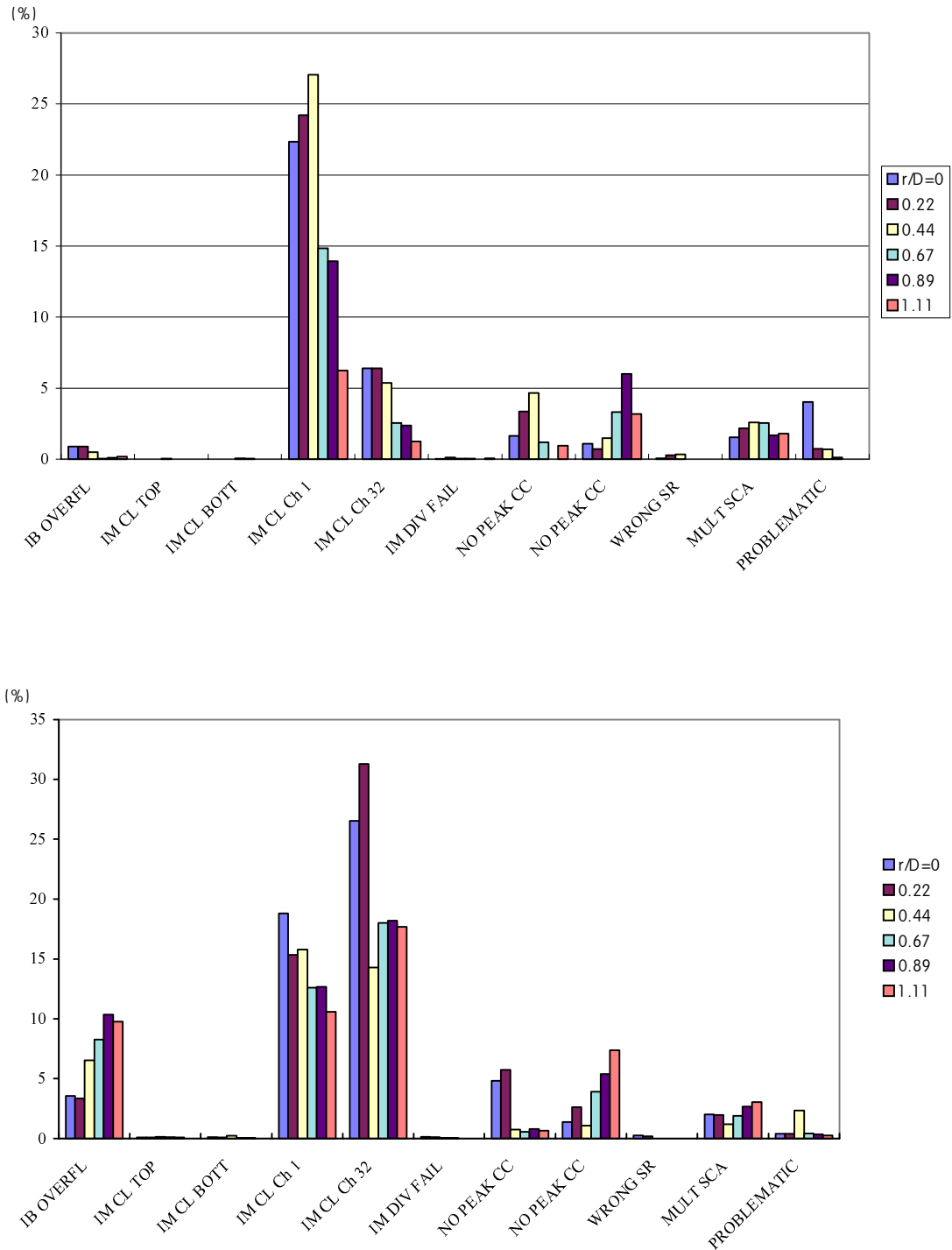


Figure 2.23 Sources of rejection of measurements by SDV along a radial profile, determined from measurement in the burner of Chapter 4 for  $S=0.41$ , at  $z/D=2.67$  (top) and  $z/D=4$  (bottom). The values of the ordinate are explained in Table 2.3.

contribution to the total rejection rate. It is evident that the most important source is rejection due to image clipping along the detector, and it is likely to be due to:

- Large particles passing off-centre of the detector, thus covering a full half-length of the array and resulting in rejection.
- Beam wandering that yields voltage output levels from the extreme channels below 75% of the value corresponding to maximum local irradiance (as determined during “referencing”), which is misinterpreted by the signal processor as a shadow.

Provided that particle flow is not omni-directional as, for example, in the region of stagnation points in recirculating flows, reduction of the magnification ratio would result in smaller shadow images on the detector and therefore reduction of occurrence of image clipping along the detector. In omni-directional flows there is always a high probability that the velocity vector of some particles will be near-parallel to the photodiode array resulting in rejection of the measurement. Reduction of the magnification ratio is realisable in particle suspensions where the size dynamic range does not exceed 10:1, the limit of the current SDV detector; in flows like pulverised-coal flames, where the usual particle distribution contains sizes between a couple of microns up to 100  $\mu\text{m}$  or more, or equivalently a dynamic range in excess of 30:1, a compromise has to be made as to which sizes it is desirable to measure. In the present thesis, the magnification ratio was adjusted to measure down to about 10  $\mu\text{m}$ , because –on the grounds of Stokes numbers defined in Chapter 4– it is likely that all particles smaller than 10  $\mu\text{m}$  will follow the flow details, a result confirmed by the work of Orfanoudakis (1994). Thus, there is little to gain by such measurements as far as particle velocity is concerned. In addition, larger particles carry most of flux and, thus, they are of higher importance to burner stability and emissions.

Beam wandering is a consequence of refractive index gradients along the axis of propagation of the laser beams; the latter occur and are noticeable with the SDV in reacting flows such as the swirl burners of this work. Because the photodiode array is shorter than the magnified and projected LDV probe volume, the effect of beam wandering results in data rejection due the Gaussian distribution of the illuminating laser beams. A method to reduce the influence of beam wandering without increasing the magnification ratio (because that would affect the measurable size range) is to use a cylindrical transmitting lens, as in the case of the water tunnel flow of this chapter, to increase the width of the LDV probe volume along the detector, and thus, reduce spatial irradiance gradients due to Gaussian distribution that result in data rejection because of beam wandering.

## 2.9 Summary of Experimental Uncertainties

The uncertainties on the measurement of particle size and flux based on the previous work are shown in Table 2.4 and are briefly summarised under the next three subheadings.

### Size Uncertainties in Open Isothermal Flows

The random uncertainty in the measurement of the size of a single particle was smaller than 6% and the random uncertainty in the mean size became insignificant with increasing sample size (§2.6.4). Morikita *et al.* (1995) have confirmed the accuracy of size measurement of irregular particles in isothermal flows who showed that the maximum difference between the measured mean diameter and microscopic measurement was 10%.

### Size Uncertainties in Reacting or Confined Flows

Temperature gradient effects in reacting flows result in beam wandering and Hishida *et al.* (1995) have measured a maximum 4% size underestimation in Bunsen burner flames. Extrapolating their results they concluded that this error would not exceed -15% with increasing

Table 2.4 Summary of Experimental Uncertainties with SDV

		Source	Systematic	Random
open flows		Size uncertainty in open isothermal flows		
		Size of single particle		6%
		Mean size of sample		10%
Effect of beam wandering and of windows		Mean Size uncertainty due to Beam wandering (Hishida <i>et al.</i> 1995):		
		in Bunsen burner flame	-4%	
		in large flames, extrapolated	-15%	
		Size uncertainty of 15 mm-wide optical windows (Hishida <i>et al.</i> 1995):		
		of a 25 $\mu\text{m}$ particle (pinhole) <sup>†</sup>	-12%	
	of a particle larger than 25 $\mu\text{m}$ <sup>†</sup>	-5%		

<sup>†</sup> These uncertainties depend on the size of window relative to the particle size under consideration and are due to deterioration of image quality because of the presence of the window. See Hishida *et al.* (1995) for details.

flame size. The influence of windows is to block part of the scattered light by diffraction thus resulting in less sharp shadow images on the detector plane. Hishida *et al.* (1995) also measured the effect of a 15 mm wide window behind a 25  $\mu\text{m}$  pinhole on the sizing uncertainty and found a maximum systematic underestimation of 12%. This decreased to less than -5% for scatterers larger than 25  $\mu\text{m}$  and wider windows, which is also the case in the measurements presented in Chapter 4.

### Uncertainty of Estimation of Sampling-Space Area and of Flux Measurement

The uncertainty in determining the area of the sampling space included random contributions of 7% from estimation of the defocus distance and of 3% of the width of the sampling space due to the discretisation of measurement of the particle position along the detector. The total

uncertainty in the measurement of flux was 14% which included 8% systematic uncertainty, whilst random uncertainties did not contribute because their significance decreases with increasing size of samples used in the measurement of average quantities, according to the central limit theorem.

### 2.10 Summary of Chapter 2

The principle and operation of a shadow Doppler velocimeter instrument, which is an imaging technique, for measuring the size, velocity and the volume (mass) flux of particles of arbitrary shape simultaneously were described in this chapter. The text focused on the description of the associated hardware and the method of processing the raw images in software, the method and accuracy of measuring particle volume flux, and the effect of biasing on the measured particle velocity distribution due to limitations of the present photodetector. The SDV signal processor was combined with a zero-crossings counter which processed particle velocity signals conditionally on shadow images being detected by the photodiode array. The main findings from work presented in this chapter are summarised below.

The cross-sectional area of the sampling-space of SDV measurement is geometrically defined unlike, for example, phase Doppler anemometry and amplitude-based techniques, in which the effective cross-sectional area for flux measurement depends on the amplitude of scattered light. This difference renders flux measurement using SDV more robust than the equivalent measurement with phase Doppler anemometry. The accuracy of particle flux and volume fraction was assessed from measurement in a constant-velocity turbulent water-channel flow and it was found that the maximum departure from the actual particle flux was smaller than 20% and typically 10%, for particulate volume fractions in the flow of up to 0.05%. Of this, random uncertainties of 12% were attributable to the integration procedure used in the estimation of the flux, and a systematic 8% and a further 6% to the inaccuracy in the determination of the cross-sectional area of the sampling-space and in the measurement of the particle volume respectively.

A Monte-Carlo simulation was performed in order to estimate the influence of velocity- and trajectory angle-limitations of the present photodetector on the measured velocity distributions. Two Gaussian pdfs for the axial and the radial velocity were sampled and only velocities which were within the limitations were included in the calculation of the velocity pdfs. Parametric studies for the mean and the rms axial velocity showed that the additional uncertainty in the estimation of the mean axial velocity was typically 10% whilst for the mean radial, rms radial and rms axial velocity these were about 5%.

Comparison between size- and velocity-validated data (included bias effects) and only velocity-validated data (excluded bias effects) obtained in the swirl burner of chapter 4 for swirl number 0.41, at  $r/D=0$  and  $z/D=2.67$ , showed that the uncertainty attributed to the bias effects was about 5%.

Statistical analysis of rejected measurements made across radial profiles at  $z/D=2.67$  and  $z/D=4$  in the burner of chapter 4, for swirl number 0.41, indicated that the largest contribution to the total number of rejected measurements from the SDV was from those images which were vignetted by the edges of the detector and amounted up to 20-30% of the total rejected data. It was suggested that the rejections were due to large particles or due to beam wandering caused by refractive index gradients in the reacting flow.

